Research Square

Preprints are preliminary reports that have not undergone peer review.
They should not be considered conclusive, used to inform clinical practice,
or referenced by the media as validated information.

Energy performance assessment of functionally graded metal foams using a finite element approach

Moises Guillermo Quintanilla
Universidad Nacional Autónoma de México
Ian Guillermo Monsivais
ian.monsivais@ingenieria.unam.edu
Universidad Nacional Autónoma de México
Federico Mendez
Universidad Nacional Autónoma de México

Research Article

Keywords: open-cell metal foam, functionally graded porous media, local thermal non-equilibrium, convective heat transfer, performance evaluation criterion

Posted Date: November 10th, 2026

DOI: https://doi.org/10.21203/rs.3.rs-10899678/v1

License: This work is licensed under a Creative Commons Attribution 4.0 International License.
Read Full License

Additional Declarations: No competing interests reported.

Energy performance assessment of functionally graded metal foams using a finite element approach

Moisés Quintanilla[1], Ian Guillermo Monsivais[1*†], Federico Méndez[1†]

[1*]Facultad de Ingeniería, Universidad Nacional Autónoma de México, Av. Universidad 3000, Ciudad Universitaria, 04510, Ciudad de México, México.

*Corresponding author(s). E-mail(s): ian.monsivais@ingenieria.unam.edu;
Contributing authors: m.quintanilla@comunidad.unam.mx; fmendez@unam.mx;
†These authors contributed equally to this work.

Abstract

Open-cell metal foams hold significant potential as functionally graded porous media for heat transfer applications such as solar thermal collectors; however, manufacturing constraints often limit the use of idealized, smoothly graded materials. While multiple uniform-layer foams present a pragmatic alternative, their thermohydraulic performance across moderate-to-high porosities remains under-researched. This study evaluates the energy performance of fluid flow through a parallel channel embedded with step-gradient metal foams. The Finite Element Method (FEM) was utilized to solve the normalized mass, momentum, and energy conservation equations under the Local Thermal Non-Equilibrium (LTNE) condition, examining constant, double, triple, and linear configurations at average porosities ($\overline{\phi}$) of 0.7, 0.8, and 0.9. Fluid dynamically redistributes to maintain a uniform longitudinal pressure decrease, yielding steep velocity gradients near boundaries and layer interfaces. An analysis of the non-equilibrium parameter (**ΔNE**) justifies the LTNE approach, demonstrating that thermal equilibrium is compromised near heated walls and porosity-variation interfaces. Thermally, deliberate foam stacking steepens near-wall temperature gradients and reduces the plate-to-fluid temperature difference. Notably, equal-thickness triple-layer configurations (model T2) exhibited an increase in the Performance Evaluation Criterion (PEC) of approximately 10–11% compared to the constant-porosity case at $\overline{\phi} = \mathbf{0.8}$ and **0.9**. These results suggest that strategically stacked discrete-porosity open-cell metal foams provide a highly practical approach for optimizing energy performance in convective heat exchange devices.

Keywords: open-cell metal foam, functionally graded porous media, local thermal non-equilibrium, convective heat transfer, performance evaluation criterion

Acknowledgments

Moisés Quintanilla gratefully acknowledges the support provided by the *Secretaría de Ciencia, Humanidades, Tecnología e Innovación* (SECIHTI, previously known as CONAHCYT) México, through a doctoral scholarship awarded for the period 2023–2027, under the code 6515-0587-981d-c20c-7db9-2dbd.

List of symbols

a_{sf}	specific surface area (m^{-1})
A_{sf}	area of the solid-fluid interface (m^2)
Bi_H	channel height Biot number (—)
c_F	Forchheimer drag coefficient
c_p	specific heat at constant pressure (J/kg-K)
h	heat transfer coefficient (W/m^2-K)
k	thermal conductivity (W/m-K)
K	intrinsic permeability (m^2)
p	intrinsic pressure (Pa)
Pr	Prandtl number (—)
q	heat flux absorbed by the plate (W/m^2)
Re_H	channel height Reynodls number (—)
T	temperature (K)
U_L	heat loss transfer coefficient (W/m^2-K)
u	longitudinal velocity component (m/s)
v	transversal velocity component (m/s)
V	representative elemental volume (m^3)
μ	dynamic viscosity of the fluid (Pa·s)
ρ	density (kg/m^3)
σ	phase, either fluid or solid
ϕ	porosity

1 Introduction

With energy demand projected to increase by around 1% every year [1] and the supply of fossil fuels and their derivatives being compromised in times of conflict [2], the need for systems with higher energy efficiency becomes clearer. Heat dissipation techniques for processes in which heat flux is less than 100 W/cm^2 commonly involve natural or forced convection of air and water [3]. Applications include, for example, heat removal in logic chips [4], condensation of refrigerants in HVAC [5], or heating in solar thermal collectors [6]. As a consequence, porous media have gained relevance in recent times, especially open-cell metal foams [7, 8], due to their high surface-area-to-volume ratio, high thermal conductivity, low weight (i.e., high porosity), and non-deformable structure [1, 9, 10]. Another aspect to consider is the tortuosity of the medium, defined as the ratio between the length of the path traveled by a particle and the direct distance [11], which affects thermal dispersion due to flow mixing at the pore scale in the foam, especially at high Reynolds numbers [12].

These micro-scale interactions are key to enhancing momentum and energy transfer in porous media, and specifically metal foams; however, it is very well established in literature that a macroscopic effect emerges when applying this passive method, that is, a pressure gradient penalty [13, 14]. Although this gradient reduces for a partially filled channel, the greatest increase in heat transfer occurs in fully filled flows [9]. Research reports this increase in heat transfer to be substantial and highly correlated to Reynolds numbers [15]; thus, these results may cause a bias to prioritize research on high Reynolds number cases to obtain even higher Nusselt numbers. In applications where denser fluids pass through a porous medium at lower velocities, such as in solar thermal collectors, the pore Reynolds number may be in the order of 10^1 or lower [16, 17], flow characteristics are different from those at high velocities, hence high Reynolds numbers [18]. To optimize energy efficiency without increasing pressure gradients, functionally graded metal foams emerged as a promising alternative [19]. This coincides with the recommendatinos of Pati et al. [20] to address the research gap on achieving energy efficiency. Different manufacturing techniques have been developed to produce graded material, but those that may produce foams with a smooth gradient are rather expensive and not readily available. In some cases, the foams are produced for very specific needs, such as medical prosthetics or aerospace applications [21–23].

Given manufacturing limitations, stacked foams are presented as a feasible and pragmatic alternative; however, a significant portion of the research focuses on high-porosity foams, overlooking the potential benefit that mixing lower-porosity foams (ϕ=0.60-0.85) may have [24]. This observation may be explained by considering that a denser medium produces a higher pressure penalty, indicating that researching it may not be of immediate advantage [25]. Chen et al. [26] numerically analyzed forced convective cooling, considering samples of porosity between 0.85 and 0.95. The samples were placed along the main direction of the flow with some space in between them for different discrete heat sources; they concluded that the Nusselt number obtained for the lower porosity cases was larger than that for the higher porosity. Jadhav et al. [27] modeled partially filled circular tubes, keeping porosity constant at 90% while varying pore density. They found that decreasing the number of pores per

inch (PPI) towards the heated wall resulted in the best performance. It is worth noting that, contrary to Chen et al. [26], Jadhav et al. [27] did not consider thermal dispersion effects in their equations. Kermani et al. [28] had the objective to provide a uniform distribution of flow in fuel cells by introducing step-gradient foams; their results showed potential to enhance the power extracted from fuel cells and even proposed a procedure to fabricate functionally graded metal foams, but they did not address how heat was transferred between the phases or with the surroundings. Little experimental research regarding step-gradient foams was found. Xu and Zhao [25] conducted experiments on pool boiling in stacked metal foams of varying pore densities and thickness while maintaining a constant porosity of 0.98; their research emphasized phase change as a heat transfer enhancer, rather than convective heat transfer. Another explanation for neglecting foams with intermediate porosities (50-80%) might be that simulations may require assuming that Local Thermal Equilibrium (LTE) does not apply, considering that the intensity of the non-equilibrium condition intensifies with lower porosities [29].

Although the LTE model provides us with reasonable approximations, the non-equilibrium approach may be required under some circumstances [20, 30]. For instance, a high heat transfer coefficient between the phases (h_{sf}) would require a low temperature difference to sustain heat exchange, and vice versa [31, 32]. Since the coefficient h_{sf}, is often modeled based on some form of Reynolds number [13], the same behavior may apply; despite this, the general rule is that for a higher particle Reynolds number, the LTE condition becomes invalid [20]. Another aspect worth considering is the ratio of fluid-to-solid thermal conductivities ($\kappa' = k_f/k_s$). When the ratio is low, i.e., the solid thermal conductivity is greater, the non-equilibrium condition prevails [33, 34]. Although the LTE dependency on some parameters has been studied, a more pragmatic approach would be to quantify the condition by a non-equilibrium difference ΔNE [29]. This parameter is only one of many found in the literature to establish the criteria for assuming LTE [19, 35].

Despite recent advancements, comprehensive studies optimizing fluid flow and convective heat transfer in variable-porosity media, specifically practical, step-gradient open-cell metal foams, remain scarce. To bridge this gap, the present study employs the Finite Element Method to simulate thermofluid behavior within a parallel channel configuration under an asymmetrical heat flux boundary condition, characteristic of solar thermal collectors. The effect of spatial porosity variations across a broad interval (ϕ around 60–98%) is systematically evaluated under the Local Thermal Non-Equilibrium (LTNE) condition. Characterizing the resulting velocity and temperature distributions allows for the precise quantification of friction factors and Nusselt numbers to rigorously assess overall energy performance. Ultimately, these findings provide actionable, physics-based insights for the design of highly efficient convective heat exchange devices.

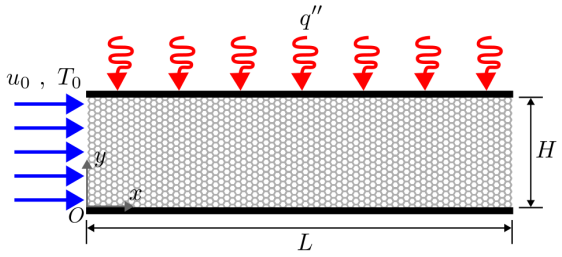


Fig. 1: Physical model.

2 Methodology

2.1 Model description

Fig. 1 depicts the model under consideration: a flow with uniform velocity and temperature enters a solar collector modeled as a parallel plate channel, which is embedded in a metal foam acting as a porous medium. The channel, with a height H and a length L, receives a uniform heat flux in the upper wall (absorber plate) while losing heat at a rate equal to the loss coefficient U_L and the local temperature difference between the plate and the surroundings. To develop the mathematical framework and define the scope of the study cases, the following assumptions were established:

- Fluid and solid properties (e.g., density, thermal conductivity, specific heat, dynamic viscosity, etc.) are constant and uniform along the domain.
- The absorber plate is made of a fine, high thermal conductivity material (e.g., a thin plate of

aluminum or copper) so that the same heat flux being absorbed at the top is transferred into the medium on the other side of the plate.

- Secondary physical effects are neglected. Internal radiation heat transfer is omitted since the expected operating temperatures in liquid-based solar collectors remain relatively low [16]. Buoyancy effects are disregarded because forced convection dictates fluid dynamics [1]. Furthermore, viscous dissipation is excluded since the working fluid operates at low velocities and small pore Reynolds numbers, rendering viscous heating negligible [34].
- Porosity varies between 0.613 and 0.978, as available experimental research shows for open-cell metal foams [36, 37]. It is worth mentioning that sintered packed beds for some metallic materials could reach porosities as low as 40% [24]; these are structurally different from metal foams, which may invalidate the models describing properties like permeability.

2.2 Mathematical modeling

2.2.1 Representative Elemental Volume (REV) approach

Throughout the literature, two approaches for treating variables inside a flow in porous media are frequently implemented: pore-scale analysis and the volume averaging technique [38, 39]; this work focuses on the latter. Considering a representative volume inside the macroscopic domain [40], the following fundamental definitions for the average volumetric quantities are established as:

$$\langle \psi_\sigma \rangle = \frac{1}{V} \int_{V_\sigma} \psi_\sigma \, dV \ , \tag{1a}$$

$$\langle \psi_\sigma \rangle^\sigma = \frac{1}{V_\sigma} \int_{V_\sigma} \psi_\sigma \, dV \ , \tag{1b}$$

where ψ is any variable describing the porous medium (e.g., pressure, temperature, longitudinal velocity, etc.) and can be used for each phase σ, which can be either the fluid (f) or solid (s) phase. Both equations are related by the following:

$$\langle \psi_\sigma \rangle = \frac{V_\sigma}{V} \, \langle \psi_\sigma \rangle^\sigma \, . \tag{2}$$

If the fluid phase is being considered (i.e., $\sigma = f$), the volume ratio becomes the porosity, $\phi = V_f/V$. To simplify the nomenclature, the macroscopic dependent variables described hereafter are defined as the volume averages of their respective quantities:

$$u = \langle u_f \rangle \ , \tag{3a}$$

$$v = \langle v_f \rangle \ , \tag{3b}$$

$$p = \langle p_f \rangle^f \ , \tag{3c}$$

$$T_f = \langle T_f \rangle^f \ , \tag{3d}$$

$$T_s = \langle T_s \rangle^s \ ; \tag{3e}$$

where u and v are the longitudinal and transverse components of the fluid velocity, respectively; p is the intrinsic fluid pressure; and T_f and T_s are the intrinsic temperatures of the fluid and solid, respectively.

2.2.2 Governing equations

The REV approach takes the spatial average operations described before and applies them to the conservation equations, namely, the continuity, Navier-Stokes, and energy equations, the latter of which is divided into two under the LTNE condition. The derivation process is analogous to that used to determine the Reynolds-Averaged Navier-Stokes equations. The implementation is well established in the literature [41, 42], and it is presented as follows. For the continuity:

$$\nabla \cdot \mathbf{v} = 0 \ . \tag{4}$$

Momentum equation:

$$\rho_f \left[\frac{\partial \mathbf{v}}{\partial t} + \left(\frac{\mathbf{v}}{\phi} \cdot \nabla \right) \left(\frac{\mathbf{v}}{\phi} \right) \right] = -\phi \nabla p + \mu \nabla^2 \mathbf{v} - \mu \left(\nabla \phi \cdot \nabla \right) \left(\frac{\mathbf{v}}{\phi} \right) - \frac{\phi \, \mu}{K} \mathbf{v} - \frac{\phi \, \rho_f \, c_F}{\sqrt{K}} |\mathbf{v}| \mathbf{v} \ . \tag{5}$$

Energy equation for the fluid:

$$\rho_f c_{p,f} \left(\phi \frac{\partial T_f}{\partial t} + \mathbf{v} \cdot \nabla T_f \right) = \nabla \cdot \left[(k_{stg,f} + \phi k_{dis}) \nabla T_f \right] + h_v \left(T_s - T_f \right) \ . \tag{6}$$

Energy equation for the solid:

$$(1-\phi)\,\rho_s c_{p,s}\frac{\partial T_s}{\partial t} = \nabla\cdot(k_{stg,s}\nabla T_s) + h_v\,(T_f - T_s)\ . \quad (7)$$

The governing system of Eqs. (4)–(7) is subsequently redefined in dimensionless form. Specifically for a 2D Cartesian coordinate system, where the velocity vector is defined as $\mathbf{v} = [u, v]$, the domain is subject to the following initial conditions:

$$u(x,y,0) = v(x,y,0) = 0\ , \quad (8a)$$
$$T_f(x,y,0) = T_s(x,y,0) = T_a\ . \quad (8b)$$

Flow velocity is conditioned at the domain boundaries as:

$$u(x,0,t) = v(x,0,t) = 0\ , \quad (9a)$$
$$u(x,H,t) = v(x,H,t) = 0\ , \quad (9b)$$
$$u(0,y,t) = u_0\ , \quad (9c)$$
$$v(0,y,t) = 0\ , \quad (9d)$$
$$\frac{\partial u(L,y,t)}{\partial x} = \frac{\partial v(L,y,t)}{\partial x} = p(L,y,t) = 0\ . \quad (9e)$$

Meanwhile, the fluid and solid temperature fields are restricted to the following boundary conditions:

$$\frac{\partial T_f(x,0,t)}{\partial y} = \frac{\partial T_s(x,0,t)}{\partial y} = 0\ , \quad (10a)$$
$$k_{stg,f}\frac{\partial T_f(x,H,t)}{\partial y} = \phi\,[q - U_L(T_p - T_a)]\ , \quad (10b)$$
$$k_{stg,s}\frac{\partial T_s(x,H,t)}{\partial y} = (1-\phi)\,[q - U_L(T_p - T_a)]\ , \quad (10c)$$
$$T_f(0,y,t) = T_0\ , \quad (10d)$$
$$\frac{\partial T_s(0,y,t)}{\partial x} = 0\ , \quad (10e)$$
$$\frac{\partial T_f(L,y,t)}{\partial x} = \frac{\partial T_s(L,y,t)}{\partial x} = 0\ . \quad (10f)$$

Initially, the fluid is at rest and in local thermal equilibrium with the solid at the ambient temperature, T_a. Because gauge pressure is being used, the pressure at the outlet is set to zero, as the flow discharges into the environment. At the upper wall, the no-slip boundary condition sets the local velocity at zero; consequently, the incident heat flux distributes between the phases in proportion to their respective effective stagnant thermal conductivities [43].

2.2.3 Models for foam properties

To solve the system of governing equations, specific macroscopic properties of metal foams must be determined. These properties are evaluated using well-established empirical models from relevant literature, as presented in Eqs. (11)–(21). The permeability of metal foams and the Forchheimer drag coefficient are formulated as [44]:

$$K = 0.00073\,d_p^2\,(1-\phi)^{-0.224}\left(\frac{d_f}{d_p}\right)^{-1.11} \quad \text{and} \quad (11)$$

$$c_F = 0.00212\,(1-\phi)^{-0.132}\left(\frac{d_f}{d_p}\right)^{-1.63}\ , \quad (12)$$

where the filament-to-pore ratio is defined as [45]:

$$\frac{d_f}{d_p} = \frac{1.18}{G}\sqrt{\frac{1-\phi}{3\pi}}\ , \quad (13)$$

and G represents a geometric shape factor:

$$G = 1 - \exp\left[-(1-\phi)/0.04\right]\ . \quad (14)$$

To evaluate heat conduction, the stagnant effective thermal conductivities are required and are formulated as follows for the fluid phase [12]:

$$k_{stg,f} = \frac{\sqrt{3}}{2}\left(\frac{r\cdot b}{\frac{2+b}{3}k_f} + \frac{(1-r)\,b}{\left(1-\frac{2b}{3}\right)k_f} + \frac{\frac{\sqrt{3}}{2}-b}{\left(1-\frac{4\,r\cdot b}{3\sqrt{3}}\right)k_f}\right)^{-1}\ , \quad (15)$$

and for the solid phase:

$$k_{stg,s} = \frac{\sqrt{3}}{2}\left(\frac{r\cdot b}{\frac{1+b}{3}k_s} + \frac{(1-r)\,b}{\frac{2b}{3}k_s} + \frac{\frac{\sqrt{3}}{2}-b}{\frac{4\,r\cdot b}{3\sqrt{3}}k_s}\right)^{-1}\ , \quad (16)$$

where

$$b = \frac{-r + \sqrt{r^2 + \frac{2\sqrt{3}}{3}(1-\phi)\left(2 - r\left(\frac{3+4\sqrt{3}}{3}\right)\right)}}{\frac{2}{3}\left[2 - r\left(\frac{3+4\sqrt{3}}{3}\right)\right]} , \tag{17}$$

and $r = 0.09$ is a constant determined to fit experimental data [12].

Thermal dispersion is defined as the spreading of heat due to hydrodynamic mixing (e.g., pore-scale velocity fluctuations, flow splitting and rejoining, and eddy formation) [34, 46]. This phenomenon is highly dependent on local velocities and, hence, on the spatial porosity distribution. Therefore, to capture this effect within the REV approach [39], thermal dispersion is pragmatically modeled in Eq. (6) as an additional effective thermal conductivity. Crucially, implementing this dispersion term in the two-equation energy conservation framework (LTNE model) prevents the volumetric interfacial heat transfer coefficient (h_v) from unrealistically inflating to compensate for the absence of thermal mixing [47]. Based on the formulations by Celik et al. [42], the longitudinal and transverse thermal dispersion components are established as follows:

$$\frac{\phi k_{dis,x}}{k_f} = \frac{0.043}{(1-\phi)^{1/4}}\sqrt{\frac{\phi}{G}}\left(\frac{u\,d_p}{\nu}\right)^{1.5} \mathrm{Pr}^{1.63} \quad \text{and} \tag{18}$$

$$\frac{\phi k_{dis,y}}{k_f} = \frac{0.000191}{(1-\phi)^{1/4}}\sqrt{\frac{\phi}{G}}\left(\frac{u\,d_p}{\nu}\right)^{1.5} \mathrm{Pr}^{1.63} , \tag{19}$$

where u represents the longitudinal velocity component, as it corresponds to the preferential flow direction.

Within the LTNE framework, the heat exchange between phases in a porous medium is mathematically established as the product of an effective heat transfer parameter and the local temperature difference between the solid and fluid, as formulated in Eqs. (6) and (7). This parameter corresponds to the volumetric interfacial heat transfer coefficient, h_v. Defined as the product of the local interfacial coefficient and the specific surface area ($h_v = h_{sf}\, a_{sf}$) [48], and it characterizes the rate of convective heat transfer between the phases of the porous medium per unit volume.

Furthermore, established empirical models do not determine this volumetric interfacial coefficient in isolation; rather, it is commonly derived through the evaluation of the volumetric interfacial Nusselt number (Nu_v) [42]:

$$\begin{aligned}\mathrm{Nu}_v &= \frac{h_v d_p^2}{k_f} \\ &= 0.94\, a_{sf}\, d_p \left(\frac{d_f}{d_p}\right)^{-0.5} \left(\frac{k_{stg,f}}{k_f}\right)^{0.63} \\ &\sqrt{\frac{u\,d_p}{\nu}} \quad \mathrm{Pr}^{0.37} .\end{aligned} \tag{20}$$

To close this formulation, the specific surface area is evaluated as [49]:

$$a_{sf} = \frac{3\pi G}{0.59^2\, d_p}\left(\frac{d_f}{d_p}\right) . \tag{21}$$

2.2.4 Dimensionless governing equations

To generalize the governing equations, a scale analysis is performed to recast the problem in dimensionless form. The independent variables x and y are scaled by the channel length L and height H, respectively:

$$\widetilde{x} = x/L \quad \text{and} \quad \widetilde{y} = y/H . \tag{22}$$

Correspondingly, the longitudinal velocity component u is normalized by the inlet velocity u_0:

$$\widetilde{u} = u/u_0 . \tag{23}$$

By expanding the continuity Eq. (4) in two dimensions, a scaling relationship is established as:

$$\frac{u_0}{L} \sim \frac{v_c}{H} , \tag{24}$$

from which the transverse characteristic velocity (v_c) is determined, thus allowing the following dimensionless variable:

$$\widetilde{v} = \frac{v}{\epsilon_L\, u_0} , \tag{25}$$

where $\epsilon_L = H/L$.

Along the preferential flow direction, momentum conservation suggests that the pressure gradient balances the Darcy term, such that:

$$\frac{\partial p}{\partial x} \sim \frac{\mu\, u}{K} \ . \tag{26}$$

Because permeability K scales with the square of the pore diameter, as in Eq. (11), the characteristic pressure drop is defined as:

$$\Delta p_c = \frac{\mu\, u_0\, L}{d_p^2} \ , \tag{27}$$

yielding the dimensionless pressure:

$$\widetilde{p} = p/\Delta p_c \ . \tag{28}$$

At the heated boundary, the absorbed heat flux distributes between the phases according to Eqs. (10b) and (10c), yielding a combined contribution scaled to a reference heat flux (q_0), such as the solar constant in solar thermal collectors:

$$k_f \frac{\Delta T_c}{H} \ , k_s \frac{\Delta T_c}{H} \sim q_0 \ . \tag{29}$$

In metal foams, because the thermal conductivity of the solid matrix is significantly larger than that of the fluid ($k_s \gg k_f$), the solid conduction term stands as the dominant contributor to the heat flux balance. Consequently, a characteristic temperature difference is defined as:

$$\Delta T_c = \frac{q_0\, H}{k_s} \ , \tag{30}$$

and the non-dimensional temperatures are established as:

$$\widetilde{\theta}_s = \frac{T_s - T_0}{\Delta T_c} \ \text{ and } \ \widetilde{\theta}_f = \frac{T_f - T_0}{\Delta T_c} \ . \tag{31}$$

Finally, to capture the pseudo-transient behavior, the time scale is governed by the dominant thermal diffusion mechanism:

$$\frac{\partial}{\partial t} \sim \frac{1}{\Delta t_c} \sim \frac{\alpha_s}{H^2} \ , \ \frac{\alpha_f}{H^2} \ . \tag{32}$$

Since the thermal diffusivity of the solid exceeds that of the fluid ($\alpha_s > \alpha_f$), the solid diffusion scale is adopted:

$$\Delta t_c = H^2/\alpha_s \ , \tag{33}$$

so that:

$$\widetilde{t} = t/t_c \ . \tag{34}$$

Applying these dimensionless variables to a 2D domain yields the normalized system of equations. For the mass conservation:

$$\frac{\partial \widetilde{u}}{\partial \widetilde{x}} + \frac{\partial \widetilde{v}}{\partial \widetilde{y}} = 0 \ . \tag{35}$$

The momentum equation along the longitudinal axis becomes:

$$\begin{aligned}
&\frac{1}{\alpha'\,\mathrm{Pr}}\frac{\partial \widetilde{u}}{\partial \widetilde{t}} + \mathrm{Re}_H \left(\epsilon_L \widetilde{u}\frac{\partial}{\partial \widetilde{x}} + \epsilon_L \widetilde{v}\frac{\partial}{\partial \widetilde{y}}\right)\left(\frac{\widetilde{u}}{\phi}\right) = \\
&\qquad -\phi\,\epsilon_p^2 \frac{\partial \widetilde{p}}{\partial \widetilde{x}} + \left(\epsilon_L^2 \frac{\partial^2 \widetilde{u}}{\partial \widetilde{x}^2} + \frac{\partial^2 \widetilde{u}}{\partial \widetilde{y}^2}\right) \\
&- \left(\epsilon_L^2 \frac{\partial \phi}{\partial \widetilde{x}}\frac{\partial}{\partial \widetilde{x}} + \frac{\partial \phi}{\partial \widetilde{y}}\frac{\partial}{\partial \widetilde{y}}\right)\left(\frac{\widetilde{u}}{\phi}\right) - \phi\,\epsilon_p^2 \left(\frac{d_p^2}{K}\right)\widetilde{u} \\
&- \phi\, c_F\, \epsilon_p\, \mathrm{Re}_H \left(\frac{d_p^2}{K}\right)^{1/2} \sqrt{\widetilde{u}^2 + \epsilon_L^2\, \widetilde{v}^2}\ \widetilde{u} \ ,
\end{aligned} \tag{36}$$

and along the transverse direction:

$$\begin{aligned}
&\frac{1}{\alpha'\,\mathrm{Pr}}\frac{\partial \widetilde{v}}{\partial \widetilde{t}} + \mathrm{Re}_H \left(\epsilon_L \widetilde{u}\frac{\partial}{\partial \widetilde{x}} + \epsilon_L \widetilde{v}\frac{\partial}{\partial \widetilde{y}}\right)\left(\frac{\widetilde{v}}{\phi}\right) = \\
&\qquad \frac{\phi\,\epsilon_p^2}{\epsilon_L^2} \frac{\partial \widetilde{p}}{\partial \widetilde{y}} + \left(\epsilon_L^2 \frac{\partial^2 \widetilde{v}}{\partial \widetilde{x}^2} + \frac{\partial^2 \widetilde{v}}{\partial \widetilde{y}^2}\right) \\
&- \left(\epsilon_L^2 \frac{\partial \phi}{\partial \widetilde{x}}\frac{\partial}{\partial \widetilde{x}} + \frac{\partial \phi}{\partial \widetilde{y}}\frac{\partial}{\partial \widetilde{y}}\right)\left(\frac{\widetilde{v}}{\phi}\right) - \phi\,\epsilon_p^2 \left(\frac{d_p^2}{K}\right)\widetilde{v} \\
&- \phi\, c_F\, \epsilon_p\, \mathrm{Re}_H \left(\frac{d_p^2}{K}\right)^{1/2} \sqrt{\widetilde{u}^2 + \epsilon_L^2\, \widetilde{v}^2}\ \widetilde{v} \ .
\end{aligned} \tag{37}$$

Dimensionless energy conservation for the fluid phase is expressed as:

$$\begin{aligned}
&\frac{\phi}{\alpha'}\frac{\partial \widetilde{\theta}_f}{\partial \widetilde{t}} + \epsilon_L\, \mathrm{Re}_H\, \mathrm{Pr} \left(\widetilde{u}\frac{\partial}{\partial \widetilde{x}} + \widetilde{v}\frac{\partial}{\partial \widetilde{y}}\right) = \\
&\qquad \epsilon_L^2 \frac{\partial}{\partial \widetilde{x}}\left(\frac{k_{stg,f} + \phi\, k_{dis,x}}{k_f}\frac{\partial \widetilde{\theta}_f}{\partial \widetilde{x}}\right) \\
&\qquad + \frac{\partial}{\partial \widetilde{y}}\left(\frac{k_{stg,f} + \phi\, k_{dis,y}}{k_f}\frac{\partial \widetilde{\theta}_f}{\partial \widetilde{y}}\right) \\
&\qquad + \mathrm{Nu}_v\, \epsilon_p^2 \left(\widetilde{\theta}_s - \widetilde{\theta}_f\right) \ ,
\end{aligned} \tag{38}$$

and for the solid:

$$(1-\phi)\,\frac{\partial\widetilde{\theta}_s}{\partial\widetilde{t}} = \epsilon_L^2\frac{\partial}{\partial\widetilde{x}}\left(\frac{k_{stg,s}}{k_s}\frac{\partial\widetilde{\theta}_s}{\partial\widetilde{x}}\right) + \frac{\partial}{\partial\widetilde{y}}\left(\frac{k_{stg,s}}{k_s}\frac{\partial\widetilde{\theta}_s}{\partial\widetilde{y}}\right) + \mathrm{Nu}_v\,\epsilon_p^2\,\kappa'\left(\widetilde{\theta}_f-\widetilde{\theta}_s\right)\ . \tag{39}$$

These formulations introduce the following dimensionless parameters:

$$\mathrm{Re}_H = \frac{u_0\,H}{\nu}\ , \tag{40a}$$

$$\mathrm{Pr} = \frac{\nu}{\alpha_f}\quad\text{and} \tag{40b}$$

$$\mathrm{Bi}_H = \frac{U_L\,H}{k_s}\ , \tag{40c}$$

$$\epsilon_p = \frac{H}{d_p}\ , \tag{40d}$$

where ϵ_p defines the pore diameter aspect ratio.

Meanwhile the property ratios and the dimensionless heat flux are defined as

$$\alpha' = \frac{\alpha_f}{\alpha_s}\ ,\ \kappa' = \frac{k_f}{k_s}\quad\text{and}\quad\widetilde{q} = \frac{q}{q_0}\ . \tag{41}$$

The initial conditions from Eqs. (8) are correspondingly redefined in dimensionless form as follows:

$$\widetilde{u}(\widetilde{x},\widetilde{y},0) = \widetilde{v}(\widetilde{x},\widetilde{y},0) = 0\ , \tag{42a}$$

$$\widetilde{\theta}_f(\widetilde{x},\widetilde{y},0) = \widetilde{\theta}_s(\widetilde{x},\widetilde{y},0) = 0\ , \tag{42b}$$

As well as the boundary conditions for the flow (Eqs. 9):

$$\widetilde{u}(\widetilde{x},0,\widetilde{t}) = \widetilde{v}(\widetilde{x},0,\widetilde{t}) = 0\ , \tag{43a}$$

$$\widetilde{u}(\widetilde{x},1,\widetilde{t}) = \widetilde{v}(\widetilde{x},1,\widetilde{t}) = 0\ , \tag{43b}$$

$$\widetilde{u}(0,\widetilde{y},\widetilde{t}) = 1\ , \tag{43c}$$

$$\widetilde{v}(0,\widetilde{y},\widetilde{t}) = 0\ , \tag{43d}$$

$$\frac{\partial\widetilde{u}(1,\widetilde{y},\widetilde{t})}{\partial\widetilde{x}} = \frac{\partial\widetilde{v}(1,\widetilde{y},\widetilde{t})}{\partial\widetilde{x}} = \widetilde{p}(1,\widetilde{y},\widetilde{t}) = 0\ , \tag{43e}$$

and for the temperatures (Eqs. 10):

$$\frac{\partial\widetilde{\theta}_f(\widetilde{x},0,\widetilde{t})}{\partial\widetilde{y}} = \frac{\partial\widetilde{\theta}_s(\widetilde{x},0,\widetilde{t})}{\partial\widetilde{y}} = 0\ , \tag{44a}$$

$$\kappa'\,\frac{k_{stg,f}}{k_f}\,\frac{\partial\widetilde{\theta}_f(\widetilde{x},1,\widetilde{t})}{\partial\widetilde{y}} = \phi\left[\widetilde{q}-\mathrm{Bi}_H(\widetilde{\theta}_p-\widetilde{\theta}_a)\right]\ , \tag{44b}$$

$$\frac{k_{stg,s}}{k_s}\,\frac{\partial\widetilde{\theta}_s(\widetilde{x},1,\widetilde{t})}{\partial\widetilde{y}} = (1-\phi)\left[\widetilde{q}-\mathrm{Bi}_H(\widetilde{\theta}_p-\widetilde{\theta}_a)\right]\ , \tag{44c}$$

$$\widetilde{\theta}_f(0,\widetilde{y},\widetilde{t}) = \frac{\partial\widetilde{\theta}_s(0,\widetilde{y},\widetilde{t})}{\partial\widetilde{x}} = 0\ , \tag{44d}$$

$$\frac{\partial\widetilde{\theta}_f(1,\widetilde{y},\widetilde{t})}{\partial\widetilde{x}} = \frac{\partial\widetilde{\theta}_s(1,\widetilde{y},\widetilde{t})}{\partial\widetilde{x}} = 0\ . \tag{44e}$$

Furthermore, the plate and ambient dimensionless temperatures are defined as:

$$\widetilde{\theta}_p = \phi\,\widetilde{\theta}_f + (1-\phi)\widetilde{\theta}_s\quad\text{and} \tag{45}$$

$$\widetilde{\theta}_a = (T_a - T_0)/\Delta T_c\ . \tag{46}$$

Applications of metal foams for heat transfer enhancement include solar thermal collectors. Experimental research carried out by Saedodin et al. [17] provides the operating conditions for a water-based solar collector filled with a copper metal foam, with pores as large as a few millimeters and a flow moving at velocities between 2 and almost 4 cm/s in a channel nearly 1 meter in length and 1.3 cm in height. Approximating these conditions results in a Re_H of around 600 and a Prandtl number of 6. Since height, length, and pore diameter are separated by about one order of magnitude, it was assumed that $\epsilon_L = 10$ and $\epsilon_p = 0.1$. Given that copper is highly conductive, the ratios of thermal diffusivity and conductivity were estimated at $\alpha' = \kappa' = 1.5\times10^{-3}$; as for the Biot number, it tends to be low and was considered to be 2.5×10^{-3}.

2.3 Numerical implementation

The Finite Element Method was implemented to solve the dimensionless system of equations. For this purpose, an open-source programming language was employed, namely, FreeFEM++, which was written in C++ to solve partial differential equations with higher execution speed [50]. Since a fractional time-step framework was used to decouple velocity and pressure from the momentum equation, the Ladyszhenskaya–Babuška–Brezzi stability condition is bypassed [51], thus allowing the use of triangular equal-order piecewise P_2

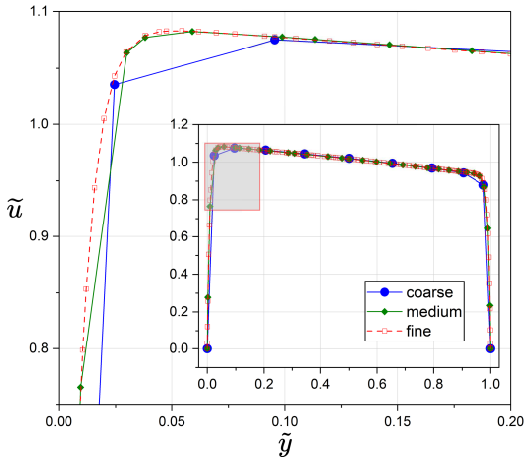


Fig. 2: Longitudinal non-dimensional velocity profile for three different mesh densities.

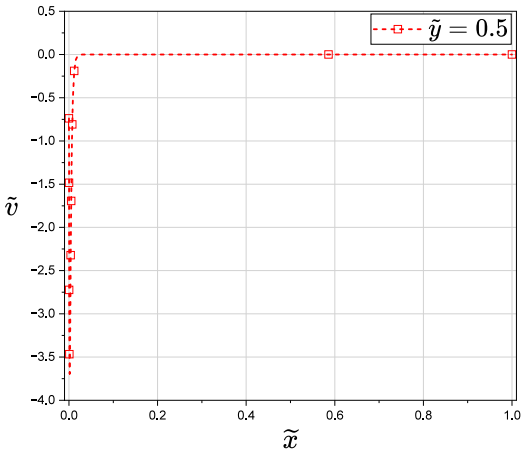


Fig. 3: Transverse non-dimensional velocity profile for the fine mesh.

continuous Lagrangian elements for all dependent variables.

Based on the procedure described by Badruddin [31], first, initial values for the dependent variables are proposed; second, flow-governing equations (continuity and momentum) are solved; third, the temperature fields, for both fluid and solid, are calculated simultaneously based on velocity results; and fourth, the convergence criteria are checked. If the error falls below a certain threshold, the iterative process ends; otherwise, the results obtained in the current iteration are used as initial guesses in the next one. Since velocity and pressure fields may converge earlier than temperatures, different criteria are defined for each phenomenon. When flow variables have converged, the program ceases to solve them; however, it continues to utilize the velocity results to solve the energy equations, as these results are independent of temperature.

To solve flow variables (namely, pressure and velocity components), a three-step temporal discretization is derived [52]: first, an auxiliary velocity solution is estimated considering only the inertial and diffusive terms of the normalized momentum equations (36) and (37); second, divergence is applied to the remaining terms to determine pressure considering continuity, Eq. (35); and third, the estimated pressure field is applied to the auxiliary velocity results as a correction [53].

A mesh refinement analysis was conducted to verify numerical accuracy. A variable-porosity

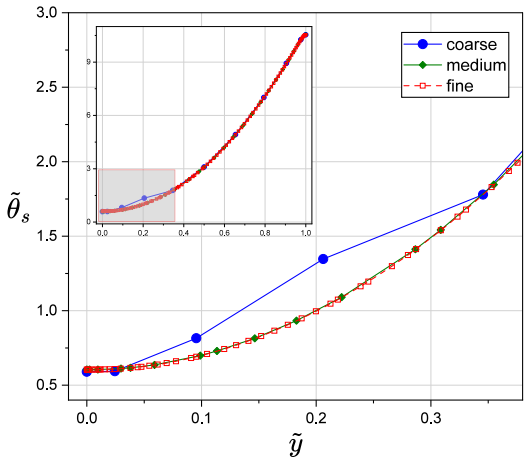
Table 1: Summary of mesh refinement analysis.

Type	Nodes	RCS[1]	f	$\overline{\mathrm{Nu}}_w$
Coarse	1681	0.071	40.202	38.379
Medium	10201	0.022	40.196	40.514
Fine	40401	0.007	40.197	40.139
Extrapolated	∞	0	40.198	40.057
$\mathrm{GCI}_{\mathrm{medium}}$			0.0018%	0.72%

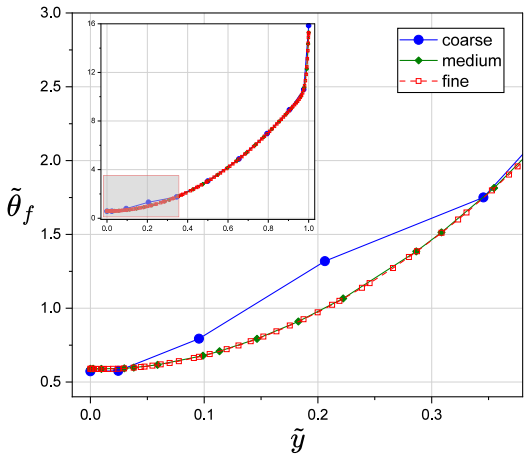
[1]Representative cell size.

case was simulated using three distinct mesh densities (coarse, medium, and fine). The coarse mesh results deviated significantly from the other two densities, as illustrated in Fig. 2, where the horizontal component of velocity is shown. Notably, Nield and Bejan [34] argue that the transverse velocity is generally of no relevance in porous media, since the hydrodynamic entry region is negligible, as corroborated in Fig. 3. Additionally, small differences in the velocity component u were found between the medium and fine meshes, particularly in regions with higher shear rates. Regarding the temperatures, the results of the coarse mesh also differ from the other two, but the medium and fine meshes give virtually the same results, a situation that can be observed in Fig. 4 for the temperature profiles for the solid and fluid regions.

To assess numerical uncertainty, simulation verification was performed in a structured and standardized manner. This procedure followed



(a) Solid temperature.



(b) Fluid temperature.

Fig. 4: Non-dimensional temperature profiles along the $\widetilde{y}$-axis in the middle of the channel ($\widetilde{x} = 0.5$) for three different mesh densities.

established literature guidelines on the Grid Convergence Index (GCI) and Richarson extrapolation [54, 55]. For this purpose, parameters representing the hydrodynamic and thermal aspects were selected. Specifically, the friction factor (f) and the average wall Nusselt number ($\overline{\mathrm{Nu}}_w$) were estimated across the three mesh densities, defined by the following relationships:

$$f = \frac{2\,\epsilon_p^2}{\mathrm{Re}_H}\,\Delta\widetilde{p} \quad \text{and} \tag{47}$$

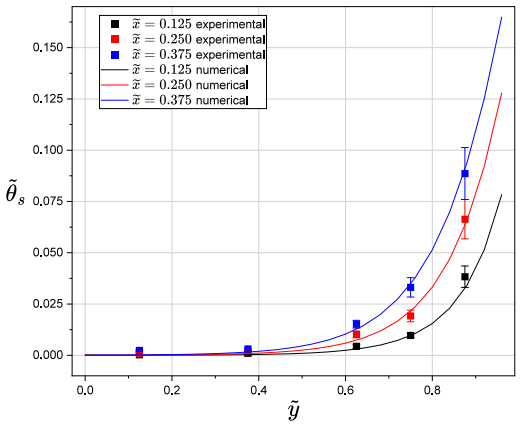


Fig. 5: Dimensionless solid temperature profiles derived from experimental data [56] compared against numerical computations for a foam with $\phi = 0.782$.

$$\overline{\mathrm{Nu}}_w = \int_0^1 \mathrm{Nu}_w\, d\widetilde{x} = \int_0^1 \frac{1}{\left(\widetilde{\theta}_p - \widetilde{\theta}_m\right)} \left(\frac{\partial\widetilde{\theta}_f}{\partial\widetilde{y}}\right)\Bigg|_{\widetilde{y}=1} d\widetilde{x}\,, \tag{48}$$

where

$$\widetilde{\theta}_m = \int_0^1 \widetilde{u}\,\widetilde{\theta}_f\, d\widetilde{y} \quad \text{and} \tag{49}$$

$$\Delta\widetilde{p} = \int_0^1 \left(\widetilde{p}_{(\widetilde{x}=0)} - \widetilde{p}_{(\widetilde{x}=1)}\right) d\widetilde{y} = \int_0^1 \widetilde{p}_{(\widetilde{x}=0)}\; d\widetilde{y}\,. \tag{50}$$

In Table 1, the values of the friction factor and average wall Nusselt number are presented for three different cases, varying the number of nodes and extrapolating to the case of an infinite number of nodes. In this table, the GCI for the medium-density mesh is reported for a safety factor of 3 [55]. For the friction coefficient, the error is negligible, and for the Nusselt number, it is less than 1%, sufficiently low for engineering applications.

Validation was accomplished by matching the experimental results documented in the literature [56], which corresponded to constant-porosity foams. Fig. 5 illustrates the solid non-dimensional temperature distribution along the $\widetilde{y}$-axis at different locations along the channel. The numerical

simulations and experimental data were found to be in reasonable agreement.

3 Results and Discussion

This study evaluates the thermo-hydraulic effects of varying porosity of metal foams using the Finite Element Method to solve the governing mass, momentum, and energy equations under the LTNE condition. The findings show that step-gradient foams redistribute flow momentum to maintain a uniform longitudinal pressure gradient, resulting in a reduced friction factor in most cases while enhancing heat transfer near heated zones. Consequently, this approach improves the PEC compared to the constant porosity benchmark.

3.1 Description of study cases

Following an approach analogous to Xu and Zhao [25], different porosity configurations of metal foams were examined to systematically assess their thermohydraulic performance. Each configuration was designed to maintain one of three specific domain-averaged porosities ($\overline{\phi} = 0.7$, 0.8, and 0.9) to encompass moderate-to-high porosity regimes. As a baseline for comparison, a single-layer, uniform-porosity metal foam (model C) was defined.

For the step-gradient configurations, the channel domain was segmented vertically into horizontally stacked, discrete layers of uniform-porosity metal foam, classified as double-layer (D) and triple-layer (T) systems. Geometrically, these composites were structured to decrease in porosity stepwise toward the heated upper wall. This orientation was motivated by recent literature [27, 57] that indicates a higher metal density near heated boundaries improves thermal performance since a denser solid matrix increases local effective thermal conductivity and facilitates heat removal from the wall. Physically, this stacking arrangement is hypothesized to optimize the thermohydraulic balance: the denser upper strata enhance near-wall heat removal, while the high-porosity lower layers reduce hydrodynamic flow resistance.

Numerical suffixes in these categories denote variations in the thickness of the bottom layer. In particular, configurations designated with the suffix '2' (i.e., D2 and T2) represent systems where all layers have the same thickness. In contrast,

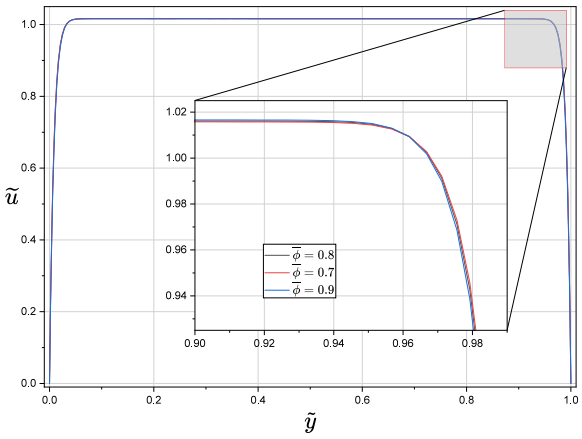


Fig. 6: Non-dimensional longitudinal velocity profile for constant porosity cases.

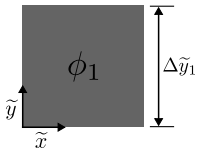
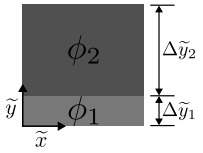
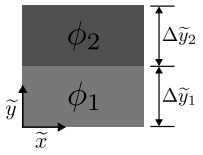
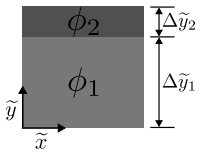
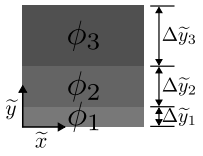
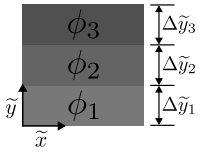
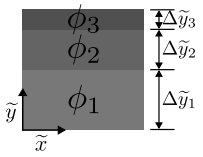
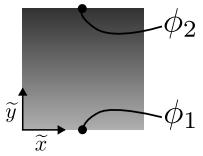
models designated with '1' and '3' represent asymmetric layer distributions, engineered to evaluate the effect of shifting the porosity-transition interface further from and closer to the heat source, respectively. The exact geometric parameters for all configurations are detailed in Table 2.

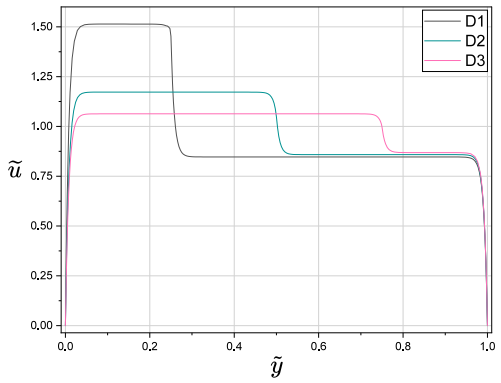
Finally, since the equal-thickness layer arrangements serve as discrete approximations of a continuous gradient, a theoretical limiting case arises when considering an infinite number of infinitesimally thin, equidistant layers. This configuration, designated as model L, is defined by a smooth, linear variation in porosity from the bottom of the channel to the top wall. It thus serves as the idealized, functionally graded benchmark against which the practical stacked models are evaluated.

3.2 Hydrodynamic characteristics

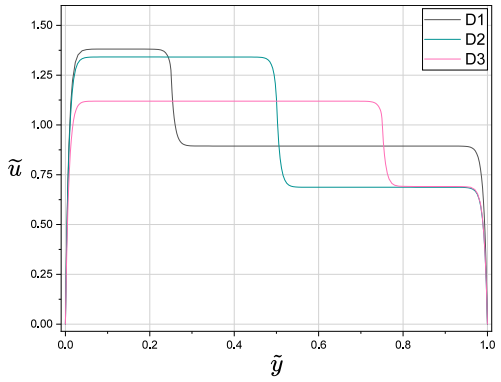
Given that the region of hydrodynamic development occurs over a relatively short region in a porous medium (see Fig. 3) [19, 34], the analysis focuses on the fully developed flow in the main channel domain. As a benchmark for comparison, the velocity distributions were determined for different constant-porosity models, as illustrated in Fig. 6. In these uniform cases, the velocity remains almost unaffected by porosity, governed by the characteristic plug-flow profile. However, a closer examination reveals that the lower porosities induce a slightly higher velocity near the walls, although this behavior is reversed at the center.

Table 2: Description of the different cases simulated in this study.

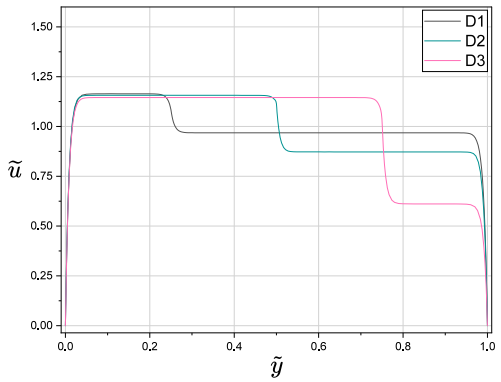
Model	Diagram	$\overline{\phi}$	$\Delta\widetilde{y}_1$	ϕ_1	$\Delta\widetilde{y}_2$	ϕ_2	$\Delta\widetilde{y}_3$	ϕ_3
C		0.7	1.0	0.7	–	–	–	–
		0.8	1.0	0.8	–	–	–	–
		0.9	1.0	0.9	–	–	–	–
D1		0.7	0.25	0.961	0.75	0.613	–	–
		0.8	0.25	0.978	0.75	$0.740\overline{6}$	–	–
		0.9	0.25	0.978	0.75	0.874	–	–
D2		0.7	0.5	0.787	0.5	0.613	–	–
		0.8	0.5	0.978	0.5	0.622	–	–
		0.9	0.5	0.978	0.5	0.822	–	–
D3		0.7	0.75	0.729	0.25	0.613	–	–
		0.8	0.75	$0.862\overline{3}$	0.25	0.613	–	–
		0.9	0.75	0.978	0.25	0.666	–	–
T1		0.7	$0.16\overline{6}$	0.961	$0.3\overline{3}$	0.7	0.5	0.613
		0.8	$0.16\overline{6}$	0.978	$0.3\overline{3}$	0.8	0.5	$0.740\overline{6}$
		0.9	$0.16\overline{6}$	0.978	$0.3\overline{3}$	0.9	0.5	0.874
T2		0.7	$0.3\overline{3}$	0.787	$0.3\overline{3}$	0.7	$0.3\overline{3}$	0.613
		0.8	$0.3\overline{3}$	0.978	$0.3\overline{3}$	0.8	$0.3\overline{3}$	0.622
		0.9	$0.3\overline{3}$	0.978	$0.3\overline{3}$	0.9	$0.3\overline{3}$	0.822
T3		0.7	0.5	0.729	$0.3\overline{3}$	0.7	$0.16\overline{6}$	0.613
		0.8	0.5	$0.862\overline{3}$	$0.3\overline{3}$	0.8	$0.16\overline{6}$	0.613
		0.9	0.5	0.978	$0.3\overline{3}$	0.9	$0.16\overline{6}$	0.666
L		0.7	–	0.787	–	0.613	–	–
		0.8	–	0.978	–	0.622	–	–
		0.9	–	0.978	–	0.822	–	–



(a) $\overline{\phi} = 0.7$

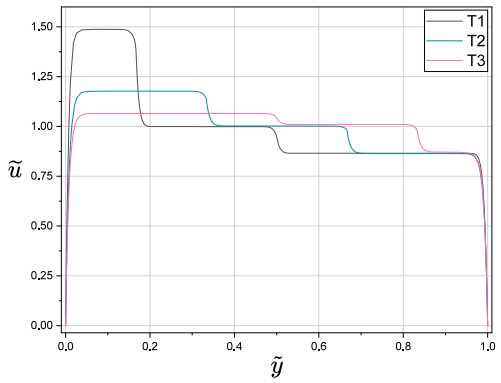


(b) $\overline{\phi} = 0.8$

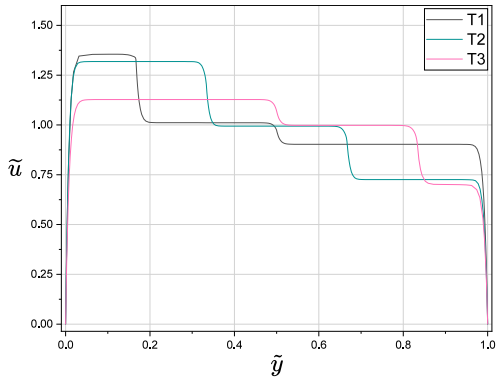


(c) $\overline{\phi} = 0.9$

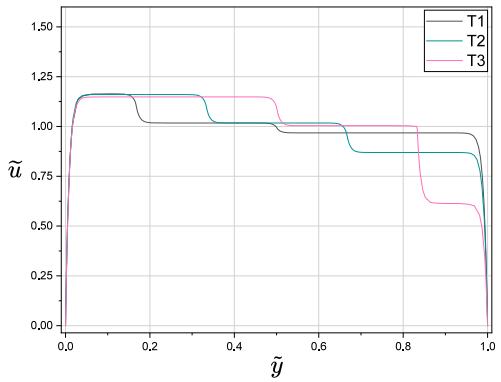
Fig. 7: Velocity profiles for double-layer models and different average porosities.



(a) $\overline{\phi} = 0.7$



(b) $\overline{\phi} = 0.8$



(c) $\overline{\phi} = 0.9$

Fig. 8: Velocity profiles for triple-layer models and different average porosities.

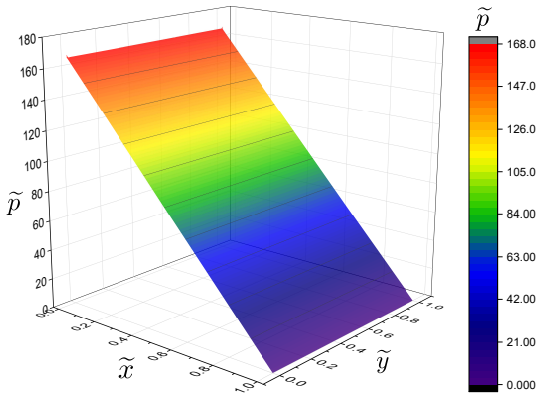


Fig. 9: Non-dimensional pressure field for model T2 and $\overline{\phi} = 0.8$.

While the velocity profiles do not change substantially, the dimensionless pressure drop (see Eq. 50) increases as porosity decreases, yielding values of 132.96, 171.63, and 215.15 for $\phi = 0.9$, 0.8, and 0.7, respectively. Furthermore, a variable porosity arrangement fundamentally disrupts the characteristic plug flow, as shown in Figs. 7 and 8.

Regions characterized by lower porosities exhibit reduced velocities along the longitudinal axis, as seen in Figs. 7 and 8. These results are in line with those of Bai et al. [19] and Jadhav et al. [27], who demonstrated that a denser solid matrix, achieved by decreasing porosity or increasing pore density, imposes flow restrictions that reduce local velocity. This hydrodynamic behavior is driven by changes in local permeability and Forchheimer drag, the primary forces opposing flow in porous media. For example, using the parameters outlined in Subsection 2.2.4 at a porosity of 0.9, the relative permeability, that is K/d_p^2 (from Eq. 11), is approximately 0.011; at $\phi = 0.7$, it decreases to 0.005, representing a reduction of over 50%. This drop in permeability, coupled with the drag coefficient, explains why, in instances with an average porosity of 0.8 for cases D2 and T2 (Figs. 7b and 8b), the velocity on the lower-porosity side is suppressed to nearly half that of the higher-porosity region.

Changes in velocity adjust the Darcy, Forchheimer, and Brinkman components within the momentum equations, ensuring that the pressure field varies along the preferential flow direction, independent of porosity configuration. As illustrated in Fig. 9, even the triple-layer system with the maximum porosity difference exhibits a linear pressure gradient along the longitudinal axis. This observation is supported by Bai et al. [19] and Kermani et al. [28]. Although fluid diverts to the high-porosity zones, this redistribution, coupled with the Brinkman viscous corrections, diminishes the velocity near the heated wall, leading to a thin thermal boundary layer, as suggested by Xia et al. [53]. To evaluate this effect, a detailed assessment of temperature distributions is necessary to validate the alteration under the LTNE condition.

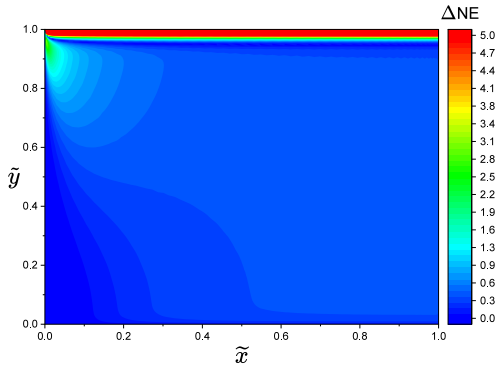
3.3 LTNE condition

Fig. 10 illustrates the non-equilibrium intensity for configurations with an average porosity of $\overline{\phi} = 0.7$. Notably, this intensity increases substantially near the heated upper wall and across regions of differing porosity. To systematically evaluate the inter-phase thermal disparity, the non-equilibrium parameter (ΔNE) introduced by Dehghan et al. [29] is adapted to the dimensionless framework presented in this paper as

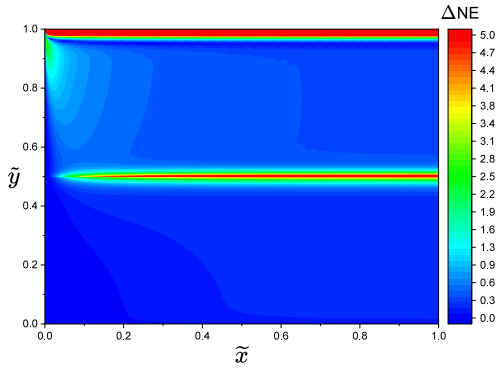
$$\Delta\mathrm{NE} = \left| \frac{\left(\widetilde{\theta}_f - \widetilde{\theta}_s\right) \kappa' \, \epsilon_p^2 \, \mathrm{Nu}_v}{2\left(\widetilde{q} - Bi_H \left(\widetilde{\theta}_p - \widetilde{\theta}_a\right)\right)} \right| . \tag{51}$$

According to Eq. (51), a substantial inter-phase temperature difference alone does not inherently guarantee a high ΔNE, since this parameter is inversely proportional to the net dimensionless heat flux. Conversely, the grouping $\kappa' \, \epsilon_p^2 \, \mathrm{Nu}_v$ represents a dimensionless interfacial heat transfer coefficient. Consequently, even if the temperature difference is minimal, a large magnitude of this coefficient can still yield an elevated ΔNE. Furthermore, because the volumetric Nusselt number (Nu_v) and local temperatures are coupled to the local fluid velocity and void fraction via Eq. (38), flow redistribution across varying-porosity regions induces a pronounced thermal mismatch between the phases. This effect locally amplifies ΔNE, as observed in Fig. 10.

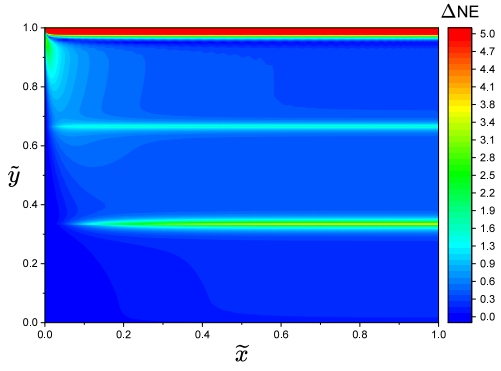
Although ΔNE remains relatively low throughout a significant portion of the domain for all evaluated cases (as indicated by the predominantly minimal contours in Fig. 10), the lowest domain-averaged ΔNE is reported for the constant-porosity case ($\phi = 0.7$) at 0.735. While Dehghan et al. [29] do not explicitly state a



(a) Case C



(b) Case D2



(c) Case T2

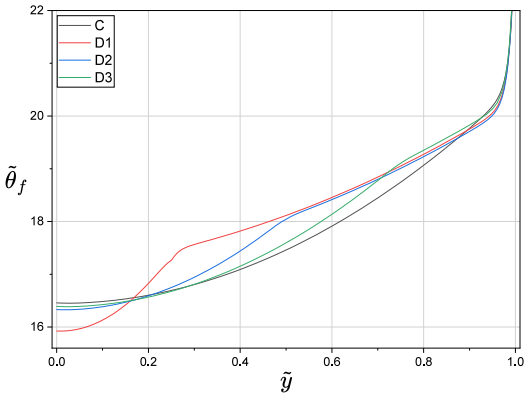
Fig. 10: Non-equilibrium difference for cases with average porosity of 0.7.

numerical threshold for the validity of the LTE approach, their analytical framework establishes that ΔNE represents the ratio of interfacial heat transfer relative to the heat flux at the boundaries. Consequently, a value of $\Delta\text{NE} = \mathcal{O}(1)$ indicates that the phases exhibit significant disparity; under these conditions, the LTE assumption is inadequate, resulting in the loss of critical thermal data. Because the domain-average values for all evaluated cases fall within this order of magnitude, the implementation of the local thermal non-equilibrium (LTNE) approach is justified.

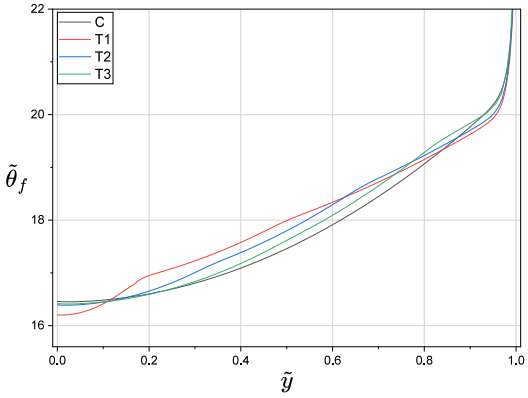
3.4 Temperature profiles

While the parameter ΔNE measures the relative thermal disparity between phases, temperatures are best illustrated in Figs. 11 and 12, which depict the fluid and solid temperature profiles at the channel outlet ($\widetilde{x} = 1.0$). Adjacent to the heated wall, the fluid temperature vastly exceeds that of the solid matrix, exhibiting a prominent gradient. This observation is in line with the discussion of Yang and Vafai [58] for a low value of $\kappa' = k_f/k_s$. Due to this relationship, the highly thermally conductive metallic material requires a mild temperature gradient to transport thermal energy. Conversely, since the fluid is less conductive, it develops a steep gradient near the wall, inducing high temperatures close to the upper boundary for all cases.

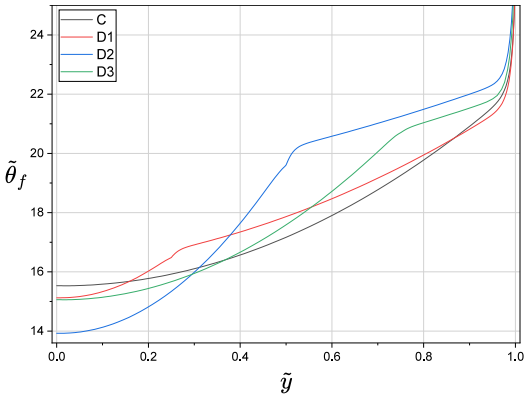
Though the solid and fluid temperatures remain relatively close, the fluid exhibits a lower temperature neral. This finding aligns with those reported by Chen et al. [13] and Wang and Guo [59]. Notably, regions where porosity varies are clearly identifiable in Figs. 11 and 12. The fluid temperatures vary gradually in those areas, resulting in smooth gradients due to convective heat transfer influenced by local velocity. As depicted in Figs. 7 and 8, the smooth transition of velocity between regions directly shapes the fluid temperature profiles. Meanwhile, solid temperature profiles exhibit abrupt transitions, since different regions have distinct effective solid thermal conductivities. The effect of variable porosity is also present in the temperature differential across the upper and lower boundaries. For models with an average void fraction of $\overline{\phi} = 0.7$, the mean difference is $(\overline{\theta}_{top} - \overline{\theta}_{bottom}) = 6.9$; conversely, for $\overline{\phi} = 0.9$, the difference roughly doubles to 14.1. This



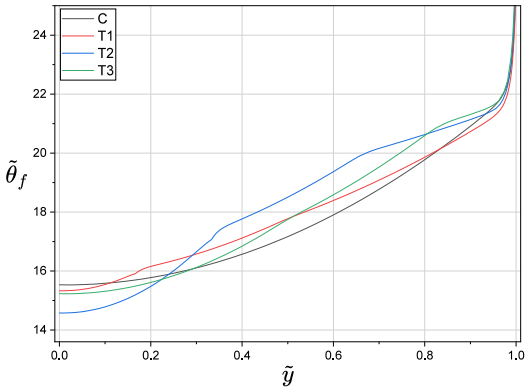
(a) Double layers, $\overline{\phi}$=0.7



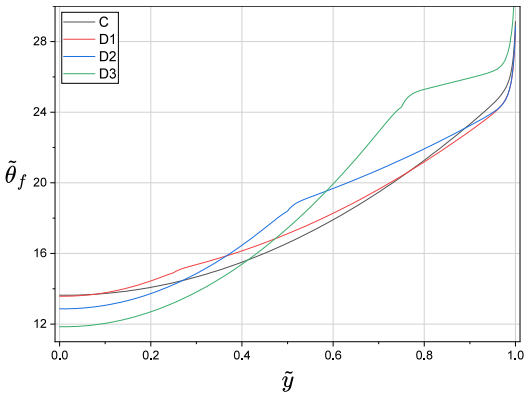
(b) Triple layers, $\overline{\phi}$=0.7



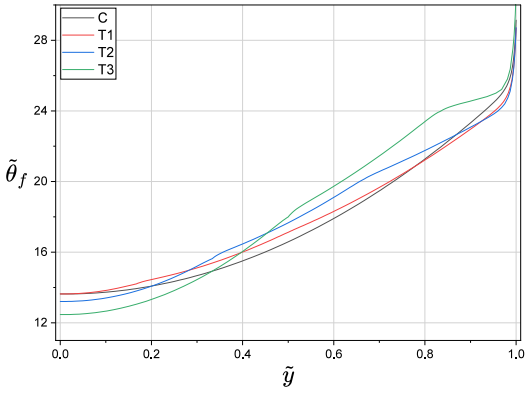
(c) Double layers, $\overline{\phi}$=0.8



(d) Triple layers, $\overline{\phi}$=0.8



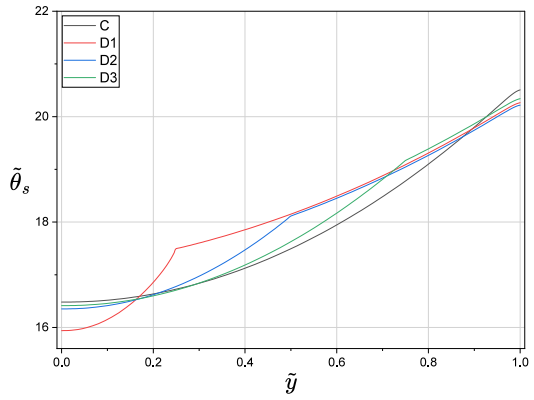
(e) Double layers, $\overline{\phi}$=0.9



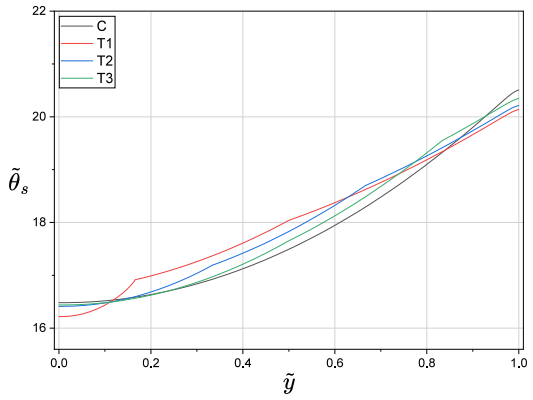
(f) Triple layers, $\overline{\phi}$=0.9

Fig. 11: Dimensionless outlet fluid temperatures.

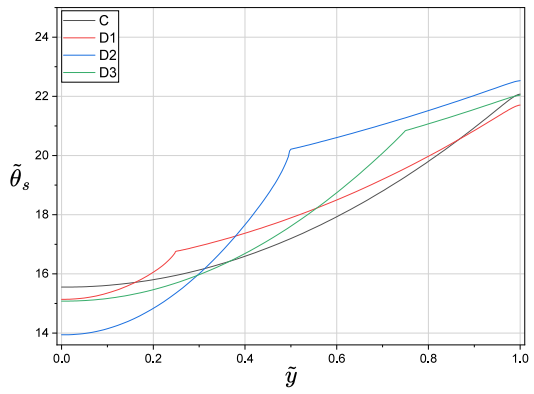
is explained by the denser metallic material at lower porosities, which enhances the overall thermal conductivity of the system, requiring a smaller temperature gradient to transfer heat transversely.



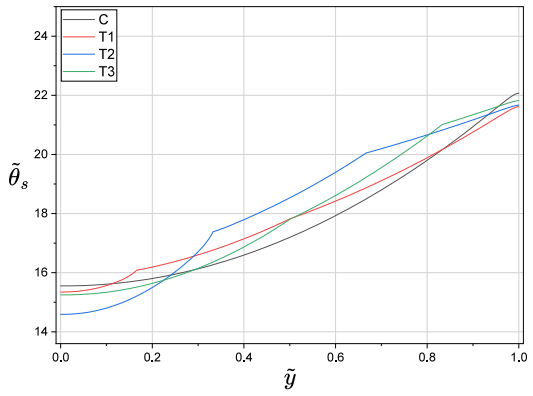
(a) Double layers, $\overline{\phi}$=0.7



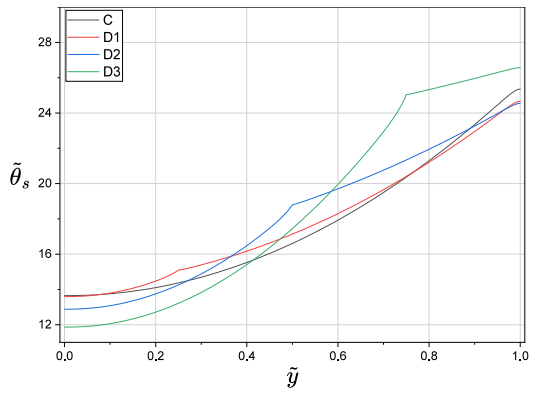
(b) Triple layers, $\overline{\phi}$=0.7



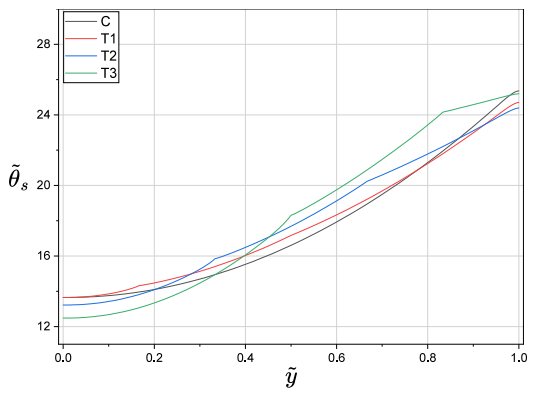
(c) Double layers, $\overline{\phi}$=0.8



(d) Triple layers, $\overline{\phi}$=0.8



(e) Double layers, $\overline{\phi}$=0.9

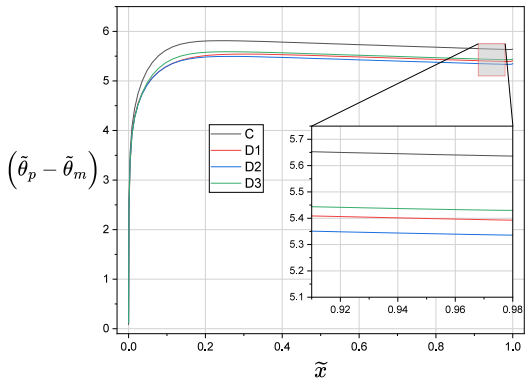


(f) Triple layers, $\overline{\phi}$=0.9

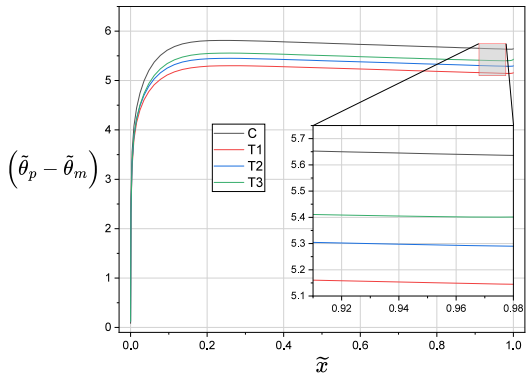
Fig. 12: Dimensionless outlet fluid temperatures.

3.5 Overall energy performance assessment

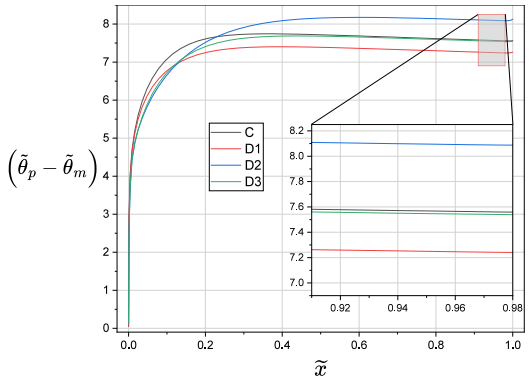
The simultaneous evaluation of both macroscopic friction factor and average wall Nusselt number



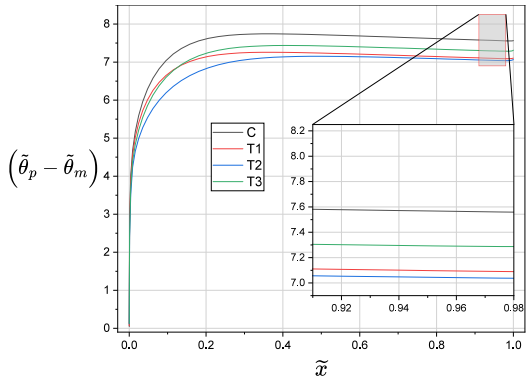
(a) Double layers, $\overline{\phi}$=0.7



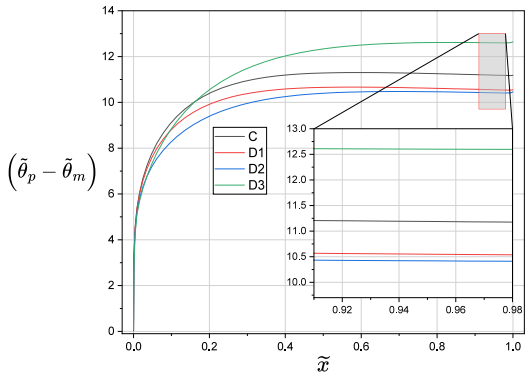
(b) Triple layers, $\overline{\phi}$=0.7



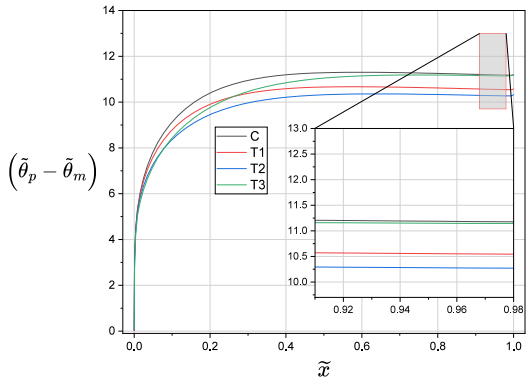
(c) Double layers, $\overline{\phi}$=0.8



(d) Triple layers, $\overline{\phi}$=0.8



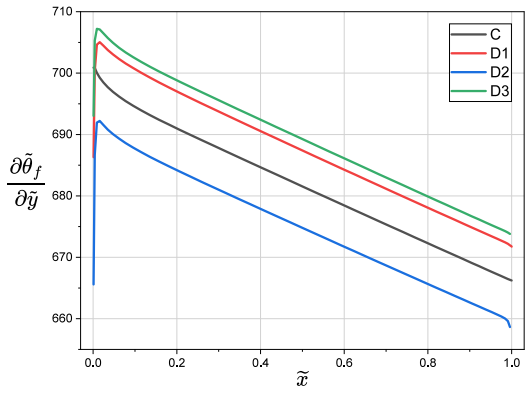
(e) Double layers, $\overline{\phi}$=0.9



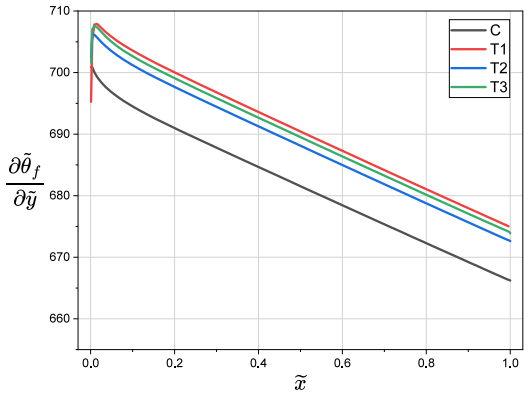
(f) Triple layers, $\overline{\phi}$=0.9

Fig. 13: Plate-to-fluid temperature difference divided by number of layers and average porosity.

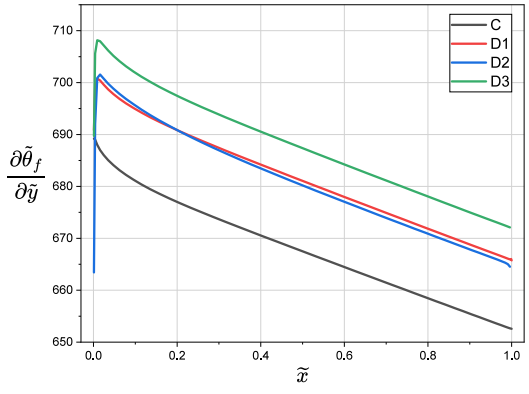
is required to fully assess the PEC. The macroscopic friction factors, determined via Eq. (47), are detailed in Table 3. These friction factors are inversely correlated with porosity, which is consistent with the findings of Ambrosio et al. [10] and Shen et al. [60]. A reduced porosity inherently obstructs the flow, leading to an elevated



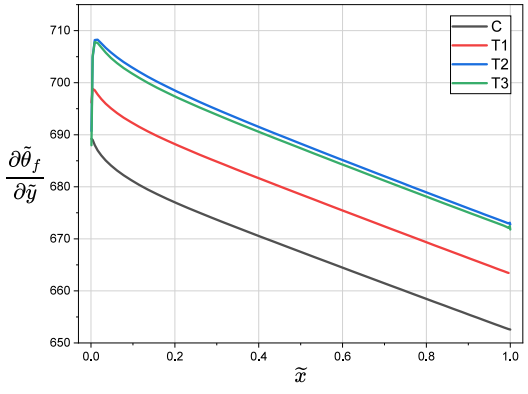
(a) Double layers, $\overline{\phi}$=0.7



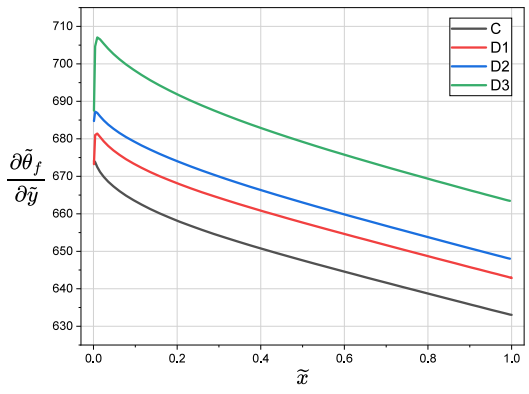
(b) Triple layers, $\overline{\phi}$=0.7



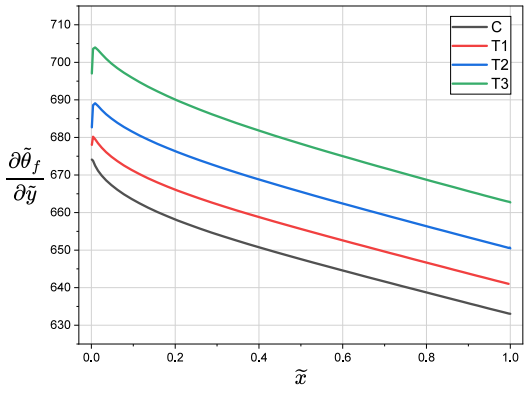
(c) Double layers, $\overline{\phi}$=0.8



(d) Triple layers, $\overline{\phi}$=0.8



(e) Double layers, $\overline{\phi}$=0.9



(f) Triple layers, $\overline{\phi}$=0.9

Fig. 14: Fluid temperatures gradient towards the system, by number of layers and average porosity.

hydrodynamic drag. To establish a comparative baseline against the constant-porosity case, the relative percentage difference is reported in Table 3 as:

$$\delta_{\%} = \frac{\Phi_M - \Phi_C}{\Phi_C} \times 100\%\,, \tag{52}$$

Table 3: Friction factors f for different porosity distributions and averages, and relative percentage difference compared to the constant porosity cases.

	$\overline{\phi} = 0.7$		$\overline{\phi} = 0.8$		$\overline{\phi} = 0.9$	
Model	f	$\delta_{\%}$	f	$\delta_{\%}$	f	$\delta_{\%}$
C	71.72	–	57.21	–	44.32	–
D1	69.34	−3.32%	56.87	−0.61%	44.39	+0.15%
D2	70.12	−2.23%	54.44	−4.85%	44.42	+0.21%
D3	71.10	−0.87%	55.26	−3.41%	43.38	−2.14%
T1	70.06	−2.32%	56.92	−0.51%	44.38	+0.12%
T2	70.57	−1.61%	55.31	−3.33%	44.43	+0.23%
T3	71.27	−0.64%	55.91	−2.28%	43.56	−1.72%
L	71.12	−0.84%	56.47	−1.29%	44.33	+0.02%

Table 4: Wall Nusselt numbers Nu_w for different porosity distributions and averages, and relative percentage difference compared to the constant porosity cases.

	$\overline{\phi} = 0.7$		$\overline{\phi} = 0.8$		$\overline{\phi} = 0.9$	
Model	$\overline{\mathrm{Nu}}_w$	$\delta_{\%}$	$\overline{\mathrm{Nu}}_w$	$\delta_{\%}$	$\overline{\mathrm{Nu}}_w$	$\delta_{\%}$
C	121.61	–	91.345	–	65.209	–
D1	127.87	5.15%	96.572	5.72%	67.609	3.68%
D2	125.45	3.16%	89.394	−2.14%	70.344	7.87%
D3	127.25	4.64%	94.803	3.79%	62.304	−4.45%
T1	134.50	10.6%	98.314	7.63%	68.086	4.41%
T2	130.64	7.43%	101.92	11.6%	70.581	8.24%
T3	127.99	5.25%	97.159	6.36%	68.022	4.31%
L	129.04	6.11%	100.62	10.2%	69.677	6.85%

Table 5: Performance Evaluation Criterion for different porosity distributions and averages.

Model	$\overline{\phi} = 0.7$	$\overline{\phi} = 0.8$	$\overline{\phi} = 0.9$
D1	1.063	1.059	1.036
D2	1.039	0.995	1.078
D3	1.049	1.050	0.962
T1	1.115	1.078	1.044
T2	1.080	1.128	1.082
T3	1.055	1.072	1.049
L	1.064	1.106	1.068

where Φ denotes either the friction factor or the average wall Nusselt number, and the subscripts M and C refer to the specific multi-layer model (e.g., D1, T2, L, etc.) and the constant-porosity benchmark, respectively.

In most of the evaluated cases, stacking layers of varying porosity reduces the overall friction factor, with double-layer configurations yielding notable decreases. These reductions manifest due to the higher-porosity regions functioning as hydrodynamic relief pathways; their elevated permeability allows the fluid bypass with low resistance. This flow diversion mechanism is effective at moderate average porosities ($\overline{\phi} = 0.7$ and 0.8), where the permeability difference between adjacent layers is highly pronounced. Consequently, flow momentum is redistributed toward the high-porosity regions, as illustrated in Figs. 7 and 8. Conversely, at a high average porosity ($\overline{\phi} = 0.9$), the permeability differential is insufficient to fully compensate for the localized drag induced within the lower-porosity segments, yielding only marginal, detrimental variations in the overall friction factor (Table 3).

The wall Nusselt number characterizes the ratio of convective to conductive heat transfer at the system boundary [29]. Thus, the plate-to-fluid temperature difference $\left(\widetilde{\theta}_p - \widetilde{\theta}_m\right)$ must be rigorously examined (Fig. 13). Jadhav et al. [61] demonstrated that wall temperatures escalate at higher porosities, a trend corroborated by the present plate-to-fluid temperature differences. For instance, the mean differential for case C at $\overline{\phi} = 0.7$ nearly doubles that observed at $\overline{\phi} = 0.9$. However, in model D2 at $\overline{\phi} = 0.8$ (Fig. 13c) and model D3 at $\overline{\phi} = 0.9$ (Fig. 13e), the temperature difference exceeds the constant-porosity benchmark. This deviation is primarily attributed to severe permeability transitions at the layer interfaces. This abrupt hydrodynamic transition surpresses transverse thermal dispersion, locally stagnate the fluid, and elevate residency times adjacent to the heated wall, thereby exacerbating the plate-to-fluid temperature differences. However, this disruption is attenuated in the triple-layer cases, since they exhibit a smoother transition in the velocity distribution.

Within the open-cell metal foam systems presented, an increase in the average void fraction leads to milder fluid temperature gradients near the heated boundary, while the layered models show gradients steeper than their corresponding constant-porosity benchmarks (see Fig. 14). This diverges from the findings of Bai et al. [19], although they assumed local thermal equilibrium and implemented different models to evaluate the effective thermal conductivity and other relevant properties. A minor exception occurs in model D2 at $\overline{\phi} = 0.7$ (see Fig. 14a), which demonstrates a negligible decrease in the gradient of approximately 1–2%. However, this reduction is compensated by a simultaneous drop in the plate-to-fluid temperature difference (Fig. 13a), which ultimately yields an increase in the average plate Nusselt number (Table 4). This specific case highlights that the localized reduction of fluid availability near the heated boundaries is, by itself, insufficient to fully explain the steepened temperature gradient; hence, the porosity and macroscopic flow distribution strongly influence the heat conduction from the wall to the system.

The wall Nusselt numbers reported in Table 4 show an overall increase with porosity. This trend is consistent with the findings of Iasiello et al. [57], who argue that a denser metallic matrix near the heated boundary enhances the Nusselt number. However, this explanation is incomplete. In the cases (such as model D1) where the layer adjacent to the heated boundary has the lowest porosity and spans a larger portion of the channel, the maximum Nusselt numbers are not achieved. In fact, the thickness of the near-wall layer does not strictly correlate with the Nusselt number, as the highest values are reported in the triple-layer arrangements.

Analyzing the peak Nusselt numbers requires a focused evaluation of the triple-layer models. At $\overline{\phi} = 0.7$, the fluid temperature gradients across the triple-layer arrangements (Fig. 14b) exhibit similar magnitudes; thus, model T1 yields the highest Nusselt number due to its minimized plate-to-fluid temperature difference (Fig. 13b). For average porosities of 0.8 and 0.9, models T2 and T3 demonstrate the steepest near-wall temperature gradients. While model T3 achieves a slightly steeper gradient than T2 at $\overline{\phi} = 0.9$ (Figs. 14d and 14f), model T2 consistently maintains a lower plate-to-fluid temperature difference within the developing region of the channel (Figs. 13d and 13f). The superior thermal performance of the equal-thickness T2 configuration over the asymmetrical T3 configuration is physically governed by the equidistant velocity boundary layer transitions. This uniform distribution of the layers of equal thickness forces a more sustained, uniform disruption of the thermal boundary layer, thus favoring continuous localized mixing. This enhanced thermal dispersion (k_{dis}) penetrates further into the core sections of the flow and efficiently reduces the temperature difference between the plate and fluid, without restricting the flow momentum. Interestingly, an idealized functionally graded case (model L) does not achieve the highest Nusselt number, demonstrating that discrete, macroscopic flow disruptions imposed by stepped interfaces are critically important for enhancing convective transport.

Finally, the overall energy optimization is quantified by the PEC, which captures both the Nusselt number and friction factor variations [18,

57, 62, 63], as defined in the following equation:

$$\mathrm{PEC} = \frac{(\mathrm{Nu}_w/\mathrm{Nu}_{w,C})}{(f/f_C)^{1/3}}, \tag{53}$$

where the subscript C denotes the constant-porosity baseline. The obtained PEC values are reported in Table 5 and are mainly driven by the trends of the Nusselt number, since the thermal changes are much larger than the variations of the hydrodynamic friction. For open-cell metal foams with $\overline{\phi} = 0.7$, model T1 provides the optimal PEC by positioning a dense solid matrix next to the heat source and maintaining a smooth transition of the velocity in the bulk flow. Notably, the equal-thickness triple-layer configuration (model T2) is the best overall for the average porosities of 0.8 and 0.9.

4 Conclusions

This study evaluates the energy performance of fluid flow through a parallel plate channel system, operating under conditions representative of a solar thermal collector embedded with a step-gradient open-cell metal foam. The macroscopic synthesis of the multi-layer models reveals that the fluid velocity distribution adapts to maintain the uniform longitudinal pressure gradient characteristic of channel flow. In particular, the flow accelerates in the regions of higher porosity due to the reduced Forchheimer drag and increased permeability, yielding steep velocity gradients close to the no-slip boundaries and the layer interfaces. Furthermore, while the non-equilibrium parameter (ΔNE) remains relatively low across the majority of the domain, the assumption of Local Thermal Equilibrium (LTE) is compromised near the heated boundary and adjacent to the porosity-variation interfaces, justifying the essential need for the non-equilibrium approach to capture these localized thermal variances.

The implementation of vertically stacked foams provides a highly practical approach for influencing the fluid temperature distribution to optimize energy performance. Fluid temperatures exhibit a steep gradient adjacent to the heated wall in all evaluated cases, including the constant-porosity base case. Simultaneously, the plate-to-fluid temperature difference reduces in most multi-layer systems. However, in certain configurations, the transverse fluid temperature difference expands, reducing overall energy efficiency compared to the constant-porosity reference case. Notably, the highest peak performance is obtained for the equal-thickness triple-layer configuration (model T2), indicating that the deliberately stacked discrete, uniform-porosity metal foams improve the Performance Evaluation Criterion (PEC) by approximately 10–11%. Further studies must overcome the limitations of the present study to completely characterize these optimized models. Moreover, since the present analysis assumes a strictly low-velocity regime, in which viscous dissipation is negligible, future studies should investigate the sensitivity of the system performance to wider ranges of the channel-height Reynolds number, the thermal conductivity ratio, the Prandtl number, and geometric variables.

Statements and Declarations

Authors contribution

Conceptualization: Moisés Quintanilla, Ian Guillermo Monsivais, Federico Méndez; Methodology: Moisés Quintanilla; Software: Moisés Quintanilla; Validation: Moisés Quintanilla; Formal Analysis: Moisés Quintanilla; Investigation: Moisés Quintanilla; Writing - Original Draft: Moisés Quintanilla; Writing - Review & Editing: Ian Guillermo Monsivais, Federico Méndez; Supervision: Ian Guillermo Monsivais, Federico Méndez; Visualization: Moisés Quintanilla.

Funding

No direct funding was received for conducting this study.

Conflict of interest

The authors have no competing interests to declare that are relevant to the content of this article.

Data Availability

The datasets generated and/or analyzed during the current study are available from the corresponding author on reasonable request.

References

[1] Chen, K., Guo, L., Wang, H.: A review on thermal application of metal foam. Science China Technological Sciences **63**(12), 2469–2490 (2020) https://doi.org/10.1007/s11431-020-1637-3

[2] Chia, O., Edser, N.: Petrol and diesel prices continue to rise as concerns grow over us-iran ceasefire. BBC (2026)

[3] Liu, X., Yang, J., Zou, Q., Hu, Y., Li, P., Tan, L., Miljkovic, N., Yang, R.: Enhancing liquid–vapor phase-change heat transfer with micro/nano-structured surfaces. ACS Nano **19**(10), 9513–9589 (2025) https://doi.org/10.1021/acsnano.4c15277

[4] Bar-Cohen, A., Asheghi, M., Chainer, T.J., Garimella, S.V., Goodson, K., Gorle, C., Mandel, R., Maurer, J.J., Ohadi, M., Palko, J.W., Parida, P.R., Peles, Y., Plawsky, J.L., Schultz, M.D., Weibel, J.A., Joshi, Y.: The icecool fundamentals effort on evaporative cooling of microelectronics. IEEE Transactions on Components, Packaging and Manufacturing Technology **11**(10), 1546–1564 (2021) https://doi.org/10.1109/TCPMT.2021.3111114

[5] Kandlikar, S.G.: Flow boiling in minichannels and microchannels. In: Heat Transfer and Fluid Flow in Minichannels and Microchannels, pp. 175–226. Elsevier, ??? (2006). https://doi.org/10.1016/B978-008044527-4/50007-4

[6] Al-Tabbakh, A.A.: Numerical transient modeling of a flat plate solar collector. Results in Engineering **15**, 100580 (2022) https://doi.org/10.1016/j.rineng.2022.100580

[7] Badruddin, I.A., Azeem, Yunus Khan, T.M., Ali Baig, M.A.: Heat transfer in porous media: A mini review. Materials Today: Proceedings **24**, 1318–1321 (2020) https://doi.org/10.1016/j.matpr.2020.04.447

[8] Hasan, M.H., Saihood, R.G.: Experimental study on the performance of gradient pores density metal foam in a rectangular channel. Heat Transfer **54**(3), 2127–2139 (2025) https://doi.org/10.1002/htj.23248

[9] Ali, R.M.K., Lafta Ghashim, S.: Numerical analysis of the heat transfer enhancement by using metal foam. Case Studies in Thermal Engineering **49**, 103336 (2023) https://doi.org/10.1016/j.csite.2023.103336

[10] Ambrosio, G., Bianco, N., Chiu, W.K.S., Iasiello, M., Naso, V., Oliviero, M.: The effect of open-cell metal foams strut shape on convection heat transfer and pressure drop. Applied Thermal Engineering **103**, 333–343 (2016) https://doi.org/10.1016/j.applthermaleng.2016.04.085

[11] Tamayol, A., Bahrami, M.: Transverse permeability of fibrous porous media. Physical Review E **83**(4), 046314 (2011) https://doi.org/10.1103/PhysRevE.83.046314

[12] Calmidi, V.V., Mahajan, R.L.: Forced convection in high porosity metal foams. Journal of Heat Transfer **122**(3), 557–565 (2000) https://doi.org/10.1115/1.1287793

[13] Chen, X., Xia, X., Sun, C., Wang, F., Liu, R.: Performance evaluation of a double-pipe heat exchanger with uniform and graded metal foams. Heat and Mass Transfer **56**(1), 291–302 (2020) https://doi.org/10.1007/s00231-019-02700-3

[14] Kotresha, B., Gnanasekaran, N.: Numerical simulations of fluid flow and heat transfer through aluminum and copper metal foam heat exchanger – a comparative study. Heat Transfer Engineering **41**(6-7), 637–649 (2020) https://doi.org/10.1080/01457632.2018.1546969

[15] Al-Chlaihawi, K., Hasan, M., Ekaid, A.: Optimization of thermo-hydraulic performance in partially copper-foam-filled rectangular channels: Experimental insights on foam layer configurations. International Journal of Thermofluids **25**, 101032 (2025) https://doi.org/10.1016/j.ijft.2024.101032

[16] Park, S.-H., Seo, D.-H., Jeong, J.H.: Experimental and numerical analysis of thermal flow in open-cell porous metal during darcy-forchheimer transition regime. Applied Thermal Engineering **181**, 116029 (2020) https://doi.org/10.1016/j.applthermaleng.2020.116029

[17] Saedodin, S., Zamzamian, S.A.H., Nimvari, M.E., Wongwises, S., Jouybari, H.J.: Performance evaluation of a flat-plate solar collector filled with porous metal foam: Experimental and numerical analysis. Energy Conversion and Management **153**, 278–287 (2017) https://doi.org/10.1016/j.enconman.2017.09.072

[18] Wang, H., Guo, L., Chen, K.: Theoretical and experimental advances on heat transfer and flow characteristics of metal foams. Science China Technological Sciences **63**(5), 705–718 (2020) https://doi.org/10.1007/s11431-019-1455-0

[19] Bai, X., Kuwahara, F., Mobedi, M., Nakayama, A.: Forced convective heat transfer in a channel filled with a functionally graded metal foam matrix. Journal of Heat Transfer **140**(111702) (2018) https://doi.org/10.1115/1.4040613

[20] Pati, S., Borah, A., Boruah, M.P., Randive, P.R.: Critical review on local thermal equilibrium and local thermal non-equilibrium approaches for the analysis of forced convective flow through porous media. International Communications in Heat and Mass Transfer **132**, 105889 (2022) https://doi.org/10.1016/j.icheatmasstransfer.2022.105889

[21] Sanjeeviprakash, K., Kannan, A.R., Shanmugam, N.S.: Additive manufacturing of metal-based functionally graded materials: Overview, recent advancements and challenges. Journal of the Brazilian Society of Mechanical Sciences and Engineering **45**(5), 241 (2023) https://doi.org/10.1007/s40430-023-04174-1

[22] Wan, T., Liu, Y., Zhou, C., Chen, X., Li, Y.: Fabrication, properties, and applications of open-cell aluminum foams: A review. Journal of Materials Science & Technology **62**, 11–24 (2021) https://doi.org/10.1016/j.jmst.2020.05.039

[23] Yi, Z., Xiao-yun, Z., Ke, W., Si-yuan, H., Jia-gui, L., Wei, Z., Xiao-lu, G., Jin, Y.: Fabrication of functionally radial graded metallic foam. Materials Letters **264**, 127292 (2020) https://doi.org/10.1016/j.matlet.2019.127292

[24] Lu, X.: Fluid Flow and Heat Transfer in Porous Media Manufactured by a Space Holder Method. Springer Theses. Springer, Cham (2020). https://doi.org/10.1007/978-3-030-53602-2

[25] Xu, Z.G., Zhao, C.Y.: Enhanced boiling heat transfer by gradient porous metals in saturated pure water and surfactant solutions. Applied Thermal Engineering **100**, 68–77 (2016) https://doi.org/10.1016/j.applthermaleng.2016.02.016

[26] Chen, C.-C., Huang, P.-C., Hwang, H.-Y.: Enhanced forced convective cooling of heat sources by metal-foam porous layers. International Journal of Heat and Mass Transfer **58**(1-2), 356–373 (2013) https://doi.org/10.1016/j.ijheatmasstransfer.2012.11.041

[27] Jadhav, P.H., Gnanasekaran, N., Mobedi, M.: Analysis of functionally graded metal foams for the accomplishment of heat transfer enhancement under partially filled condition in a heat exchanger. Energy **263**, 125691 (2023) https://doi.org/10.1016/j.energy.2022.125691

[28] Kermani, M.J., Moein-Jahromi, M., Hasheminasab, M.R., Wei, L., Guo, J., Jiang, F.M.: Development of a variable-porosity metal-foam model for the next fuel cells flow-distributors. International Journal of Hydrogen Energy **47**(7), 4772–4792 (2022) https://doi.org/10.1016/j.ijhydene.2021.11.058

[29] Dehghan, M., Valipour, M.S., Saedodin, S.: Perturbation analysis of the local thermal non-equilibrium condition in a fluid-saturated porous medium bounded by an isothermal channel. Transport in Porous Media **102**(2), 139–152 (2014) https://doi.org/10.

1007/s11242-013-0267-2

[30] Dehghan, M., Jamal-Abad, M.T., Rashidi, S.: Analytical interpretation of the local thermal non-equilibrium condition of porous media imbedded in tube heat exchangers. Energy Conversion and Management **85**, 264–271 (2014) https://doi.org/10.1016/j.enconman.2014.05.074

[31] Badruddin, I.A.: Numerical analysis of thermal non-equilibrium in porous medium subjected to internal heating. Mathematics **7**(11), 1085 (2019) https://doi.org/10.3390/math7111085

[32] Settar, A., Nebbali, R., Madani, B., Abboudi, S.: Numerical investigation of convective heat transfer in a plane channel filled with metal foam under local thermal non-equilibrium. Mechanics & Industry **16**(5), 504 (2015) https://doi.org/10.1051/meca/2015035

[33] Alhusseny, A.N.M., Nasser, A., Al-zurfi, N.M.J.: High-porosity metal foams: Potentials, applications, and formulations. In: Ghrib, T.H. (ed.) Porosity - Process, Technologies and Applications. IntechOpen, London (2017). Chap. 8. https://doi.org/10.5772/intechopen.70451

[34] Nield, D.A., Bejan, A.: Convection in Porous Media, 5ta edn. Springer, Cham (2017). https://doi.org/10.1007/978-3-319-49562-0

[35] Kim, S.J., Jang, S.P.: Effects of the darcy number, the prandtl number, and the reynolds number on local thermal non-equilibrium. International Journal of Heat and Mass Transfer **45**(19), 3885–3896 (2002) https://doi.org/10.1016/S0017-9310(02)00109-6

[36] Du Plessis, P., Montillet, A., Comiti, J., Legrand, J.: Pressure drop prediction for flow through high porosity metallic foams. Chemical Engineering Science **49**(21), 3545–3553 (1994) https://doi.org/10.1016/0009-2509(94)00170-7

[37] Elayiaraja, P., Harish, S., Wilson, L., Bensely, A., Lal, D.M.: Experimental investigation on pressure drop and heat transfer characteristics of copper metal foam heat sink. Experimental Heat Transfer **23**(3), 185–195 (2010) https://doi.org/10.1080/08916150903399722

[38] Tang, Y., Wang, H., Huang, C.: Pore-scale numerical simulation of the heat transfer and fluid flow characteristics in metal foam under high reynolds numbers based on tetrakaidecahedron model. International Journal of Thermal Sciences **184**, 107903 (2023) https://doi.org/10.1016/j.ijthermalsci.2022.107903

[39] Whitaker, S.: Flow in porous media i: A theoretical derivation of darcy's law. Transport in Porous Media **1**(1), 3–25 (1986) https://doi.org/10.1007/BF01036523

[40] Whitaker, S.: The forchheimer equation: A theoretical development. Transport in Porous Media **25**(1), 27–61 (1996) https://doi.org/10.1007/BF00141261

[41] Theulings, M.J.B., Langelaar, M., Van Keulen, F., Maas, R.: Towards improved porous models for solid/fluid topology optimization. Structural and Multidisciplinary Optimization **66**(6), 133 (2023) https://doi.org/10.1007/s00158-023-03570-4

[42] Celik, H., Mobedi, M., Nakayama, A., Ozkol, U.: A numerical study on determination of volume averaged thermal transport properties of metal foam structures using x-ray microtomography technique. Numerical Heat Transfer, Part A: Applications **74**(7), 1368–1386 (2018) https://doi.org/10.1080/10407782.2018.1494936

[43] Ouyang, X.-L., Jiang, P.-X., Xu, R.-N.: Thermal boundary conditions of local thermal non-equilibrium model for convection heat transfer in porous media. International Journal of Heat and Mass Transfer **60**, 31–40 (2013) https://doi.org/10.1016/j.ijheatmasstransfer.2012.12.017

[44] Chen, X., Zhao, Y., Yu, X., Xu, J., Wang, Y., Li, W.: Suppression of the temperature fluctuation using metal foam insert in the pressure vessel during the transient operation process. Journal of Energy Storage **137**,

118599 (2025) https://doi.org/10.1016/j.est.2025.118599

[45] Calmidi, V.V.: Transport phenomena in high porosity fibrous metal foams. PhD thesis, University of Colorado, Boulder, Colorado (1998)

[46] Yang, C., Nakayama, A.: A synthesis of tortuosity and dispersion in effective thermal conductivity of porous media. International Journal of Heat and Mass Transfer **53**(15), 3222–3230 (2010) https://doi.org/10.1016/j.ijheatmasstransfer.2010.03.004

[47] Vijay, D., Goetze, P., Wulf, R., Gross, U.: Forced convection through open cell foams based on homogenization approach: Steady state analysis. International Journal of Thermal Sciences **98**, 381–394 (2015) https://doi.org/10.1016/j.ijthermalsci.2015.07.017

[48] Iasiello, M., Bianco, N., Chiu, W.K.S., Naso, V.: Anisotropic convective heat transfer in open-cell metal foams: Assessment and correlations. International Journal of Heat and Mass Transfer **154**, 119682 (2020) https://doi.org/10.1016/j.ijheatmasstransfer.2020.119682

[49] Raje, M., Dhiman, A.K.: Effect of pore density and porosity of spiral porous metal fins for waste heat extraction from exhaust gases. Heat Transfer **55**(2), 1155–1170 (2026) https://doi.org/10.1002/htj.70128

[50] Hecht, F.: New development in freefem++. Journal of Numerical Mathematics **20**(3-4), 251–266 (2012) https://doi.org/10.1515/jnum-2012-0013

[51] Bacuta, C., Monk, P.: Multilevel discretization of symmetric saddle point systems without the discrete lbb condition. Applied Numerical Mathematics **62**(6), 667–681 (2012) https://doi.org/10.1016/j.apnum.2011.07.010

[52] Zhao, M., Cheng, L.: Finite element analysis of flow control using porous media. Ocean Engineering **37**(14-15), 1357–1366 (2010) https://doi.org/10.1016/j.oceaneng.2010.07.003

[53] Xia, Y., Lin, X., Shu, Y., Cheng, Z.: Enhanced thermal performance of a flat-plate solar collector inserted with porous media: A numerical simulation study. Thermal Science and Engineering Progress **44**, 102063 (2023) https://doi.org/10.1016/j.tsep.2023.102063

[54] Celik, I., Guia, U., Roache, P.J., Freitas, C.J., Coleman, H., Raad, P.E.: Procedure for estimation and reporting of uncertainty due to discretization in cfd applications. Journal of Fluids Engineering **130**(7), 078001 (2008) https://doi.org/10.1115/1.2960953

[55] Freitas, C.J.: Standards and methods for verification, validation, and uncertainty assessments in modeling and simulation. Journal of Verification, Validation and Uncertainty Quantification **5**(2), 021001 (2020) https://doi.org/10.1115/1.4047274

[56] Dukhan, N., Chen, K.-C.: Heat transfer measurements in metal foam subjected to constant heat flux. Experimental Thermal and Fluid Science **32**(2), 624–631 (2007) https://doi.org/10.1016/j.expthermflusci.2007.08.004

[57] Iasiello, M., Bianco, N., Chiu, W.K.S., Naso, V.: The effects of variable porosity and cell size on the thermal performance of functionally-graded foams. International Journal of Thermal Sciences **160**, 106696 (2021) https://doi.org/10.1016/j.ijthermalsci.2020.106696

[58] Yang, K., Vafai, K.: Analysis of temperature gradient bifurcation in porous media – an exact solution. International Journal of Heat and Mass Transfer **53**(19), 4316–4325 (2010) https://doi.org/10.1016/j.ijheatmasstransfer.2010.05.060

[59] Wang, H., Guo, L.: Volumetric convective heat transfer coefficient model for metal foams. Heat Transfer Engineering **40**(5-6), 464–475 (2019) https://doi.org/10.1080/01457632.2018.1432045

[60] Shen, H., Liu, C., Yang, L., Wang, Y.:

Pore-scale numerical investigation on comprehensive heat transfer performance of homogeneous and graded metal foam heat sinks. Thermal Science **28**(2 Part B), 1529–1544 (2024) https://doi.org/10.2298/TSCI230725237S

[61] Jadhav, P.H., Gnanasekaran, N., Arumuga Perumal, D.: Numerical consideration of ltne and darcy extended forchheimer models for the analysis of forced convection in a horizontal pipe in the presence of metal foam. Journal of Heat Transfer **143**(1), 012702 (2021) https://doi.org/10.1115/1.4048622

[62] Li, Y., Yang, B., Gong, L., Cui, W., Yang, Y.: Machine learning prediction of thermo-hydraulic performance in gradient metal foam heat sink with microencapsulated phase change material slurry. International Journal of Heat and Mass Transfer **253**, 127610 (2025) https://doi.org/10.1016/j.ijheatmasstransfer.2025.127610

[63] Siavashi, M., Talesh Bahrami, H.R., Aminian, E.: Optimization of heat transfer enhancement and pumping power of a heat exchanger tube using nanofluid with gradient and multi-layered porous foams. Applied Thermal Engineering **138**, 465–474 (2018) https://doi.org/10.1016/j.applthermaleng.2018.04.066